

Electronic Supplementary Information (ESI) for

Thermally Activated Dynamic Gating Underlies Higher

Gas Adsorption at Higher Temperatures in Metal

Organic Frameworks

*Abhishek Sharma,¹ Nimish Dwarkanath,¹ Sundaram Balasubramanian*¹*

¹Chemistry and Physics of Materials Unit, Jawaharlal Nehru Centre for Advanced Scientific Research,
Bengaluru, India

*Email: bala@jncasr.ac.in

Contents

Section		Page No.
S1	Computational Details	4
S1.1	CO ₂ Binding Energy	4
S1.2	Ab-Initio Molecular Dynamics (AIMD) Simulation	4
S1.3	Force-Field	5
	Table S1. Force-field parameters	5
S1.3.1	Bond potential	5
S1.3.2	Angle potential	6
S1.3.3	Proper torsional potential	6
	Table S2. Details of torsional potential function and parameters	7
S1.3.4	Improper torsional potential	7
S1.4	Molecular Dynamics (MD) Simulation	7
	Figure S1. Atom types used for CID-Me MOF	8
	Figure S2. Pores in CID-Me MOF	9
S1.5	Pore Properties	10
	Table S3. Properties of pore in CID-Me MOF	10
S1.6	Adsorption Isotherm	10
S1.7	Well-Tempered Metadynamics (WTM)	12
S1.7.1	Free energy of pyridine (PY) ring rotation	12
S1.7.2	Free energy of CO ₂ diffusion	12
S1.7.3	Collective variable (CV) for CO ₂ diffusion between pores	13
	Figure S3. Schematic of free energy profile in periodic pores and position of a molecule relative to edges of two pores	14
	Figure S4. Schematic of pore edges in CID-Me MOF along path C and AC and switching function as function of distance.	15
	Table S4. WTM simulation parameters	17
S1.7.4	Estimation of rates from the free energy profile	17
S2	Results	18
S2.1	Grand Canonical Monte Carlo (GCMC) Simulation Results	18

	Figure S5. Adsorption isotherm results in experimental structures and MD snapshots.	18
S2.2	AIMD and MD Simulation Results	19
	Figure S6. Comparison of AIMD and MD simulation results with the experimental data	19
	Figure S7. Comparison of XRD patterns between the experimental structure and MD snapshots	20
	Figure S8. MD simulation results with 1 CO ₂ molecule in a pore	21
S2.3	WTM Simulations of PY Ring Rotation	22
	Figure S9. Free energy profile corresponding to rotation of PY rings	22
	Figure S10. Framework and CO ₂ dynamics during PY ring rotation	23
S2.4	WTM Simulation Results for CO ₂ Diffusion between Pores	24
S2.4.1	Only switching function (SF) as CV	24
	Figure S11. Result of only biasing the SF in WTM simulations	24
	Figure S12. Nomenclature of bpy rings, Meb gates, CV distances and pores	25
	Figure S13. Distribution of O-Zn-N-C proper torsional angle and distances along path C	26
	Figure S14. Distribution of O-Zn-N-C proper torsional angle and distances along path AC	27
S2.4.2	SF and atomic distances as CV	28
	Figure S15. Definition of distance CVs and name of Meb gates	28
	Figure S16. Results of WTM simulation for CO ₂ diffusion along path C, where both SF and a distance between Meb gates are biased.	29
	Figure S17. One dimensional free energy profile along path C	30
	Figure S18. Results of WTM simulation for CO ₂ diffusion along path AC, where SF and distances for opening of both Meb gates are biased.	31
	Figure S19. One dimensional free energy profile along path AC	32
S3	Effect of Free Energy Barrier and Temperature on HAHT	33
	Figure S20. Effect of free energy barrier and temperature on adsorption	34
S4	References	36

Section S1: Computational Details

S1.1 CO₂ Binding Energy

Binding energy value quantifies the attractiveness of a framework towards the gas molecule. We calculated the binding energy (E_{BE}) of one and of two CO₂ molecules in a pore of CID-Me (CID: coordination polymers with an interdigitated structure; 5-Me-ip: 5-methylisophthalate) MOF using,

$$E_{BE} = \frac{1}{n} (E_{MOF+nCO_2} - E_{MOF} - nE_{CO_2}), \quad (S1)$$

where, n is the number of CO₂ molecules; $E_{MOF+nCO_2}$, E_{MOF} and E_{CO_2} are the total energy of MOF+ n CO₂, MOF, and CO₂, respectively. These total energy values were obtained using periodic density functional theory (DFT) calculations. We used the QUICKSTEP¹ module of CP2K² package to optimize the geometry of the experimentally reported 300K CID-Me MOF (and MOF+ n CO₂) structure and obtained the total energy values. In this method, linear combination of atom centered Gaussian-type orbitals was used to describe Kohn-Sham molecular orbitals and the electron density was described as an auxiliary plane-wave basis set with energy cut-off of 600 Ry. All atoms were described using MOLOPT basis set in conjunction with norm-conserving Goedecker-Teter-Hutter³ (GTH) pseudopotentials. An accuracy of 10⁻⁷ was used for the self-consistent field (SCF) convergence of both inner and outer loops. For all the DFT calculations, we used the PBE⁴ exchange-correlation functional and incorporated dispersion corrections using the DFT-D3⁵ approach.

S1.2 Ab-Initio Molecular Dynamics (AIMD) Simulation

AIMD simulations were performed to understand the dynamics of different chemical groups in the CID-Me MOF. AIMD simulations are independent of system specific parameters (such as force-field) and provides accurate description (compared to classical force-field based simulations, particularly in the case of hybrid materials such as MOFs) of molecular dynamics. The distribution of bonds/angles/torsions calculated from an AIMD trajectory serves as the reference to examine the accuracy of the results from MD trajectories and to tune the force-field accordingly. We used CP2K² package to perform AIMD simulation of CID-Me MOF. A unit cell of the experimentally reported crystal structure at 300 K was used and AIMD simulation was performed till 17 ps in NVT ensemble with a time step of 0.5 fs. To maintain the temperature, CSVR⁶ (canonical sampling through velocity

rescaling) thermostat was used with time constant of 100 fs. During the AIMD simulation, the energy values were calculated using DFT (with same parameters described in S1.1).

The results of AIMD simulation are shown in Figure S6, where we observed close agreement of distribution of proper torsional angle (with central atoms Zn-O (of the metal complex) and O-C (junction of metal complex and bipyridine (bpy) linkers)) with the proper torsional angles found in the experimentally reported structure (at 300 K).

S1.3 Force-Field

We used the UFF⁷ force-field to model rigid and flexible CID-Me MOF. Based on the insights from AIMD simulations, we tuned the minimum of proper torsional potential (of the metal complex and junction of metal complex and bpy linkers) close to the experimental torsional angle value (details are in section S1.3.3). All other force-field parameters were taken from UFF force-field, as described below.

Table S1: Lennard-Jones interaction parameters (ϵ, σ), effective atomic charges (Z), and partial atomic charges (q) on atoms of CID-Me MOF and CO₂ molecule. For MOF, the q values were obtained using periodic charge equilibration (Qeq) method as implemented in the RASPA⁸ code.

Atom	ϵ (kcal/mol)	σ (Å)	Z	Force-field	q (e)
Zn	0.124	2.462	1.308	UFF ⁷	Qeq
C	0.105	3.431	1.912	UFF ⁷	Qeq
N	0.069	3.261	2.544	UFF ⁷	Qeq
O	0.06	3.118	2.300	UFF ⁷	Qeq
H	0.044	2.571	0.712	UFF ⁷	Qeq
C_CO ₂	0.054	2.8	-	TraPPE ⁹	0.7
O_CO ₂	0.157	3.050	-	TraPPE ⁹	-0.35

S1.3.1 Bond potential

For both MOF and CO₂, to represent the bond potential between atoms i and j , the harmonic oscillator potential form was used, which is represented as,

$$E_r = \frac{k_{ij}}{2} (r - r_{ij})^2, \quad (\text{S2})$$

where, r and r_{ij} are the distance and equilibrium bond length between atoms i and j , respectively, and k_{ij} is the bond stretching force constant. The r_{CH} value of 1.081 and 1.109 Å (using UFF) were used for H connected to sp^2 and sp^3 C atoms, respectively. For other bond types, the r_{ij} values were taken from the experimental crystal structure. For all bonds, k_{ij} values were calculated using,

$$k_{ij} = 664.12 \frac{Z_i Z_j}{r_{ij}^3}, \quad (\text{S3})$$

where, Z_i is the effective atomic charge on atom i (given in Table S1). For CO₂ molecule, the semi-rigid TraPPE force-field¹⁰ was used with r_{CO} of 1.16 Å and k_{CO} of 2000 kcal/mol-Å².

S1.3.2 Angle potential

To represent the angle potential between atoms of MOF, we used three-term Fourier expansion as,

$$E_\theta = k_{ijk} [C_0 + C_1 \cos \theta + C_2 \cos 2\theta], \quad (\text{S4})$$

where, $C_2 = 1/4(\sin^2 \theta_o)$, $C_1 = -4C_2 \cos \theta_o$, $C_0 = C_2(2 \cos^2 \theta_o + 1)$, θ_o is the equilibrium angle, and k_{ijk} is the angle bend force constant which is obtained as,

$$k_{ijk} = 664.12 \frac{Z_i Z_k}{r_{ik}^5} [3 r_{ij} r_{jk} (1 - \cos^2 \theta_o) - r_{ik}^2 \cos \theta_o]. \quad (\text{S5})$$

For CO₂ molecule, the harmonic angle potential model ($E_\theta = k_{ijk}(\theta - \theta_o)^2$) was used with k_{ijk} of 113.063 kcal/mol and θ_o of 180°.

S1.3.3 Proper torsional potential

The details of torsional potentials used for MOF atoms are provided in Table S2. In traditional UFF force-field ϕ_0 was not used, however, to maintain the structural integrity of CID-Me MOF, we used the experimental value for the proper torsional angles in metal coordination complex and nearby carbon atoms as a minimum of the torsional potential.

Table S2: Details of proper torsional potential form. ϕ is the proper torsional angle and ϕ_0 is the value of proper torsional angle in the experimental structure. C_O: carbon connected to oxygen; C_R: sp² carbon in the ring; and C_m: carbon of methyl group.

Central atoms	Functional form	Total V_ϕ (kcal/mol)	No of torsions per bond	V_ϕ per torsion (kcal/mol)
Zn-O	$E_\phi = V_\phi [1 - \cos(\phi - \phi_0)]$	13.475	2	6.737
Zn-N _R	$E_\phi = V_\phi [1 - \cos\{2(\phi - \phi_0)\}]$	0.000	8	0.000
N _R -C _R	$E_\phi = V_\phi [1 - \cos(2\phi)]$	13.475	4	3.368
C _R -C _m	$E_\phi = V_\phi [1 + \cos(3\phi)]$	1	6	0.16667
C _R -C _O	$E_\phi = V_\phi [1 - \cos\{2(\phi - \phi_0)\}]$	5	4	1.25
O-C _O	$E_\phi = V_\phi [1 - \cos\{2(\phi - \phi_0)\}]$	13.475	2	6.737
C _R -C _R in a ring	$E_\phi = V_\phi [1 - \cos(2\phi)]$	13.475	5	3.368
C _R -C _R between rings	$E_\phi = V_\phi [1 - \cos(2\phi)]$	5	4	1.25

S1.3.4 Improper torsional potential

Improper torsional potential $E_\omega = 2 [1 - \cos(\omega_{ijkl})]$, was applied on the sp² carbon atoms of the benzene ring. Here, ω_{ijkl} is the angle between the il axis and the ijk plane and for a given central atom i , the three angles between axes il , ij , and ik and corresponding planes were considered.

S1.4 Molecular Dynamics (MD) Simulation

To study the dynamics of empty MOF and CO₂ inside the MOF, we performed unbiased, equilibrium MD simulations in the NVT ensemble using Large-scale Atomic/Molecular Massively Parallel Simulator (LAMMPS).¹¹ For MD simulations, a super cell of size 3×3×3 was constructed by using the unit cell of experimentally reported structure. To maintain temperature, Nose-Hoover thermostat was used with 5 chains.¹² To model the flexible MOF, the UFF⁷ force-field was used with intra-framework LJ, Coulombic, bond, angle, dihedral, and improper dihedral potentials (details are in section S1.3). The CO₂ molecule was modeled using semi-rigid TraPPE force-field.¹⁰ A spherical cut-off distance of 13 Å was used with tail correction and LJ interaction between unlike atoms were obtained using Lorentz-

Berthelot mixing rule. For calculating long range Coulombic interactions, particle-particle particle-mesh method was used with a precision of 10^{-5} . With the mentioned force-field, we first minimized the structure of the framework, followed by temperature ramping for 1 ns to increase the temperature of the system (MOF or MOF+CO₂) from 1 to 300/195 K followed by 50 ns MD simulation in NVT ensemble with time step of 1 fs.

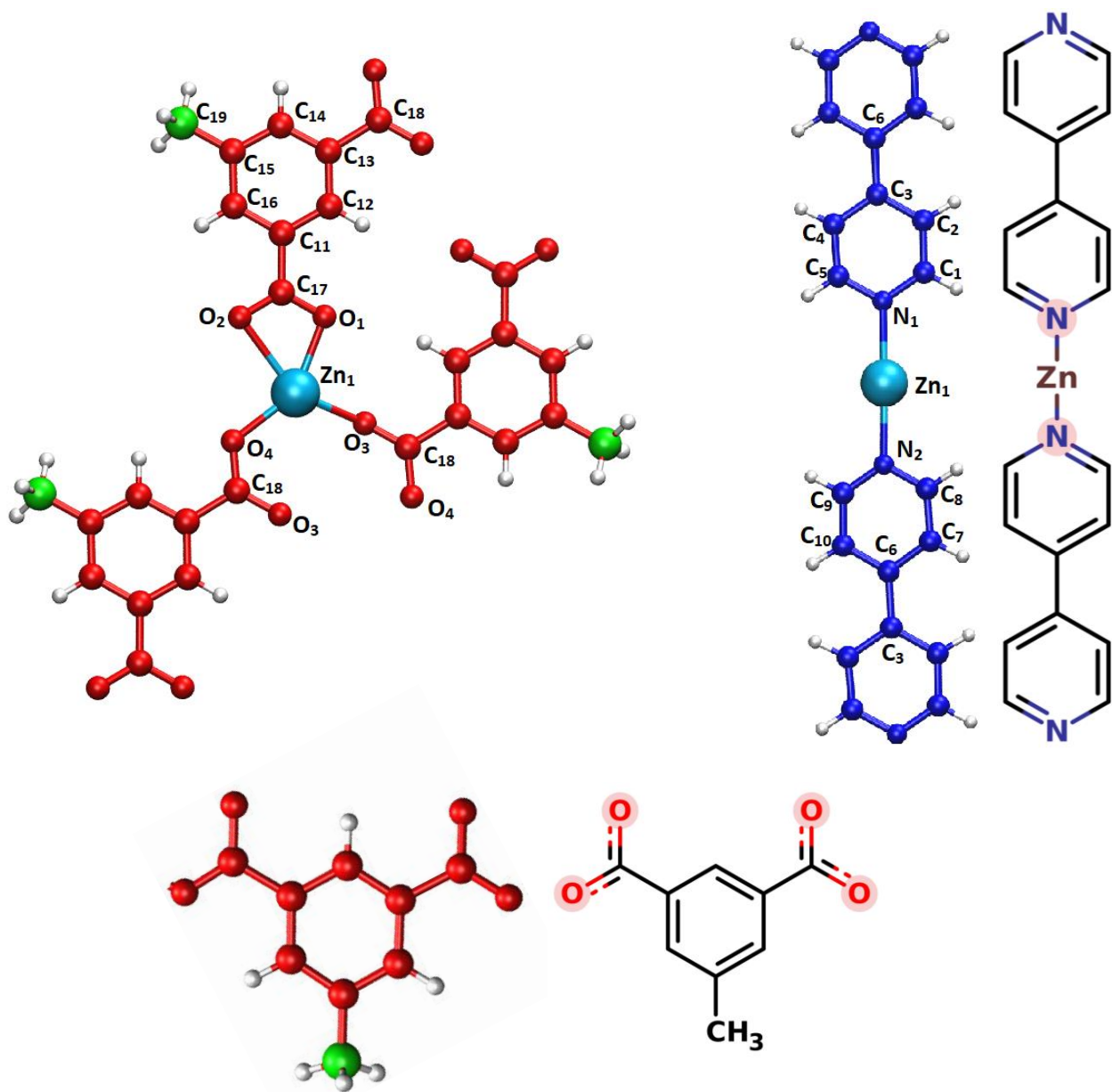


Figure S1: Atom types used for simulation of CID-Me MOF.

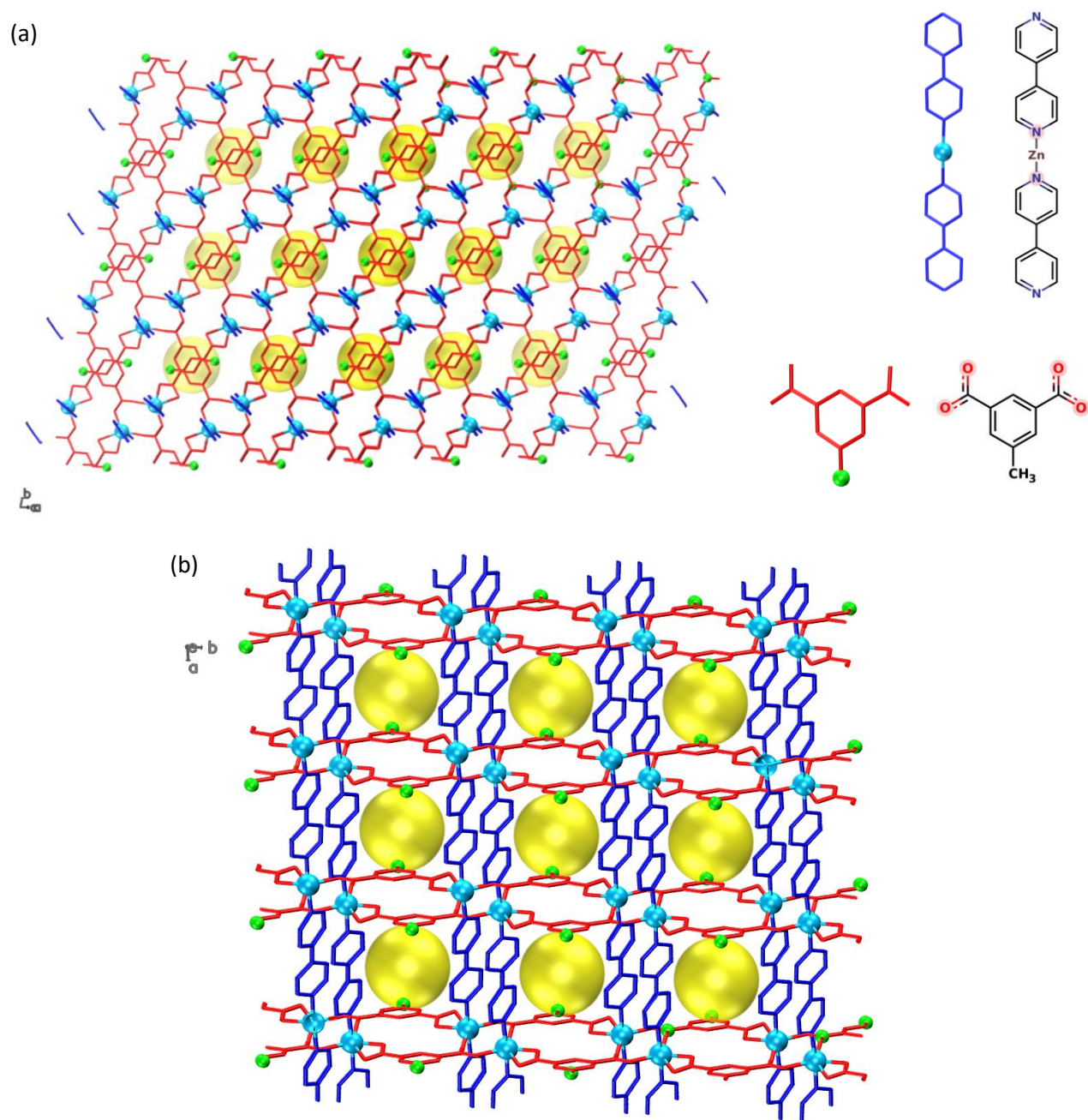


Figure S2: Structure of CID-Me MOF¹³ from different views. Blue: bipyridine (bpy), red: 5-methylisophthalate (5-Me-ip), green: methyl, cyan: zinc (Zn). Nitrogens (N) of bpy and oxygens (O) of 5-Me-ip are connected to Zn atom. Pores are shown with yellow spheres.

S1.5 Pore Properties

We calculated pore properties (i.e. pore size, surface area, and pore volume) of CID-Me metal organic framework (MOF) using Zeo++¹⁴ software with a probe of size 1.2 Å (recommended by Heerden *et al.*¹⁵). Results are given in Table S3 for pore properties of experimental structures and for the structures obtained from molecular dynamics (MD) simulations. The temperature-dependent trends exhibited by the pore properties of the experimental structure is reproduced in the flexible framework MD simulations.

Table S3: Pore properties of experimental structure (ES) and average of pore properties over 2000 molecular dynamics snapshots (< MDS >).

	Pore Size (Å)	Surface Area (m ² /g)	Pore Volume (cm ³ /g)
ES @ 195 K	3.7	467	0.012
<MDS @ 195 K>	3.95 ± 0.06	401 ± 5	0.009 ± 0.0003
ES @ 300 K	3.8	505	0.014
<MDS @ 300 K>	4.10 ± 0.08	439 ± 6	0.011 ± 0.0003

S1.6 Adsorption Isotherm

We used the unit cell of CID-Me MOF crystal structures at 195 K and 300 K as reported in experiments and obtained CO₂ adsorption isotherms (using grand canonical Monte Carlo (GCMC) simulation) in a rigid supercell (3×3×3) of both structures at respective temperatures. To account the effect of framework flexibility, we also obtained the CO₂ adsorption isotherms in five snapshots of CID-Me MOF structure (both at 195 and 300 K) generated using MD simulations (from 50 ns of MD simulation, five snapshots at 15, 20, 25,30, and 35 ns were taken). The simulated adsorption isotherm in flexible framework was obtained using the average of the simulated adsorption isotherms in MD snapshots.

To obtain adsorption isotherms, we considered rigid structures of MOF and CO₂ and performed GCMC simulations using the RASPA code.⁸ We used site-site Lennard-Jones (LJ) potential model with Coulombic interactions to model the MOF-CO₂ and CO₂-CO₂ atomic interactions. UFF⁷ and TraPPE⁹ force-field were used to describe the MOF and CO₂, respectively (see section S1.3 for details). LJ interaction parameters between unlike atoms were obtained using Lorentz-Berthelot mixing rule. For all LJ interactions, a spherical cut-off distance of 13 Å was used with tail corrections. To calculate long-

range Coulombic interactions, Ewald summation¹⁶ method was used with spherical cut-off distance of 12 Å and a precision of 10⁻⁶. Charges on MOF atoms were obtained using periodic charge equilibration method,¹⁷ as implemented in the RASPA code. During GCMC simulations, insertion, deletion, displacement, and rotation Monte Carlo (MC) move were used. In each GCMC simulation, more than 10⁵ equilibration and 10⁵ production cycles of MC moves were performed, where each cycle consists of M ($M=\max(20, \text{number of adsorbed gas molecules})$) MC moves. All simulated adsorption isotherms and their comparison with experiments is shown in Figure S5.

To understand the energetics of CO₂ adsorption, we also calculated the isosteric heat of adsorption (Q_{st}) at very low uptake using number fluctuations¹⁸ as,

$$Q_{st} = RT - \frac{\langle UN \rangle - \langle U \rangle \langle N \rangle}{\langle N^2 \rangle - \langle N \rangle^2}, \quad (\text{S6})$$

where, U is the total interaction energy (CO₂-MOF + CO₂-CO₂) and N is the number of adsorbed gas molecules.

S1.7 Well-Tempered Metadynamics (WTM)

In earlier studies on estimation of free-energy barrier for gas diffusion between pores of MOFs mainly Widom particle insertion^{19,20} and histogram sampling²¹ methods were used, considering rigid framework. In a recent study on molecular crystal **CC3**, to estimate free-energy barrier for gas diffusion between pores, Widom particle insertion (for rigid framework), implicit ligand sampling and umbrella sampling (for flexible framework) methods were used.²² To estimate gas diffusion between pores, Widom particle insertion and histogram sampling methods are useful, if there is frequent transition of gas molecules between pores via transition state during an unbiased MD/MC simulation. The implicit ligand sampling method can be used if there is no significant influence of the motion of gas molecule on the crystalline framework. In CID-Me MOF, framework dynamics is important and CO₂ transition between pores take place with the opening/closing of molecular gates, therefore Widom particle insertion, histogram sampling, and implicit ligand sampling methods are not applicable here. The umbrella sampling method requires use of many harmonic restraint potentials at different points on the diffusion path. In order to estimate the free-energy barrier for diffusion of a CO₂ molecule between neighboring pores, and to understand free-energy barrier associated with different segments (rotation of pyridine (PY) of bpy and libration of methylbenzene (Meb) of 5-me-ip groups) of CID-Me MOF, we used WTM^{23,24} method. We performed WTM simulation using the open-source community developed Plumed^{25,26} library patched with LAMMPS¹¹. In WTM simulations, a bias potential is added along the collective variable (CV), to probe the free-energy landscape along the CV.

S1.7.1 Free energy of pyridine (PY) ring rotation

For the estimation of the rotational barrier of PY ring rotation, the dihedral angle along Zn-N bond ($\phi_{O-Zn-N-C}$) was considered as a CV and the free energy profile along it was obtained using WTM. Details of WTM simulation parameters are provided in Table S4.

S1.7.2 Free energy of CO₂ diffusion

To study the transit mechanism of CO₂ between pores, we considered two paths along the *ac* (path AC) and *c* (path C) axes from a given pore and obtained free energy profiles along both the paths. Since pores in MOF are periodically connected, biasing the distance of CO₂ from the center of a pore (or any other point in the pore) would result in the CO₂ molecule moving from one unit cell to another and so

on, without the occurrence of frequent re-crossings, a feature that is essential to determine the free energy profile using WTM. Therefore, to probe the free-energy profile for the diffusion of a CO₂ molecule, we used a different type of CV (details are provided in next section).

S1.7.3 Collective variable (CV) for CO₂ diffusion between pores

In a crystalline porous material (such as a MOF), all pores are equivalent and connected (in 1D/2D/3D) in a periodic manner. In such materials, the free energy profile is also periodic according to the periodicity of pores. A typical free energy profile of a guest molecule in the pores of a crystalline porous material is schematically represented in Figure S3 (a).

To obtain the free energy profile for diffusion of CO₂ between two neighboring pores, we first defined a position vector (\vec{d}) of carbon (of CO₂) with respect to the left edge of left pore (\mathbf{L}_A) and took its component (d_a) over the vector (\vec{P}) joining the left edge of left pore (\mathbf{L}_A) and the right edge of the right pore (\mathbf{R}_B), see Figure S3 for details. This component of distance vector (d_a) describes the position of CO₂ molecule between both pores. Subsequently, we defined a switching function (SF) over d_a using Heaviside step function ($step(x_i - d_a)$) as,

$$SF(d_a) = C_1 + L_1 + C_2 + L_2$$

where,

$$C_1 = (y_{ca} - \sqrt{y_{ca}^2 - (d_a - x_1)^2}) * step(x_3 - d_a) * step(d_a - x_1)$$

$$L_1 = \frac{1}{x_5 - x_2} * (d_a - x_2) * step(x_4 - d_a) * step(d_a - x_3)$$

$$C_2 = (y_{cb} - \sqrt{(y_{cb} - 1)^2 - (d_a - x_6)^2}) * step(x_6 - d_a) * step(d_a - x_4)$$

$$L_2 = step(d_a - x_6).$$

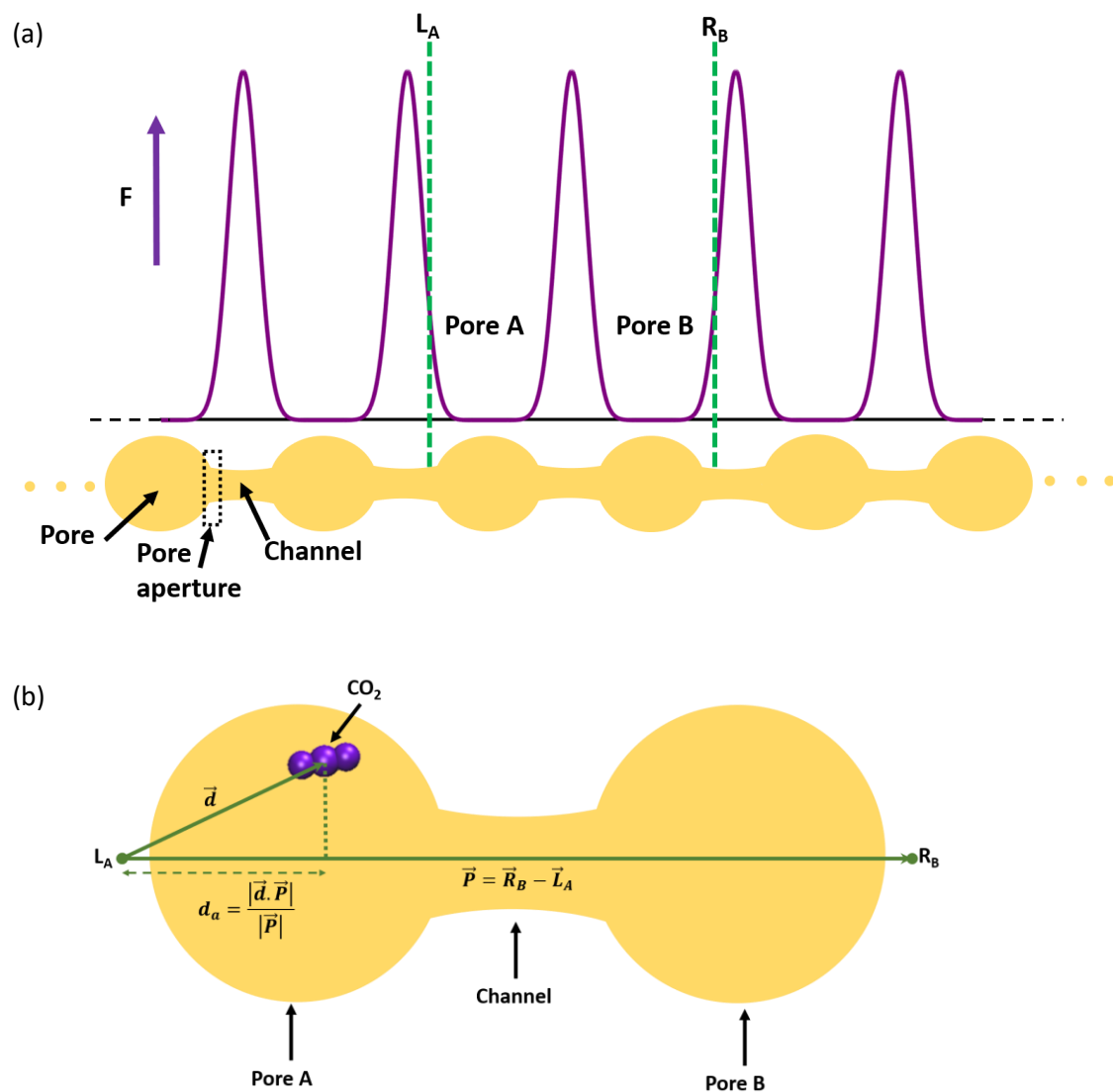


Figure S3: (a) In a porous crystal, schematic representation of periodic pores (yellow), pore aperture, channels connecting pores, and periodic free energy profile (purple) for a gas molecule to move from one pore to another pore. L_A : left edge of left pore A, R_B : right edge of right pore B. (b) Schematic representation of the position of a CO₂ molecule (violet) relative to the pores A and B, the channel connecting pore A and B, and L_A and R_B . Position of the carbon atom of the CO₂ molecule with respect to L_A is represented by \vec{d} and d_a is the component of \vec{d} along the vector connecting L_A and R_B (i.e. \vec{P}).

This SF is a smooth function of d_a (Figure S4) and varies between 0 and 1 and has one to one correspondence with d_c between 0 and $|\vec{P}|$. For all $d_a \leq 0$ (i.e., left of L_A) and $d_a \geq |\vec{P}|$ (i.e., right of R_B), SF has values 0 and 1, respectively (see Figure S4 for details). We used the SF as the collective variable (CV) to obtain the free energy profile for CO₂ diffusion between pores, as it allows the

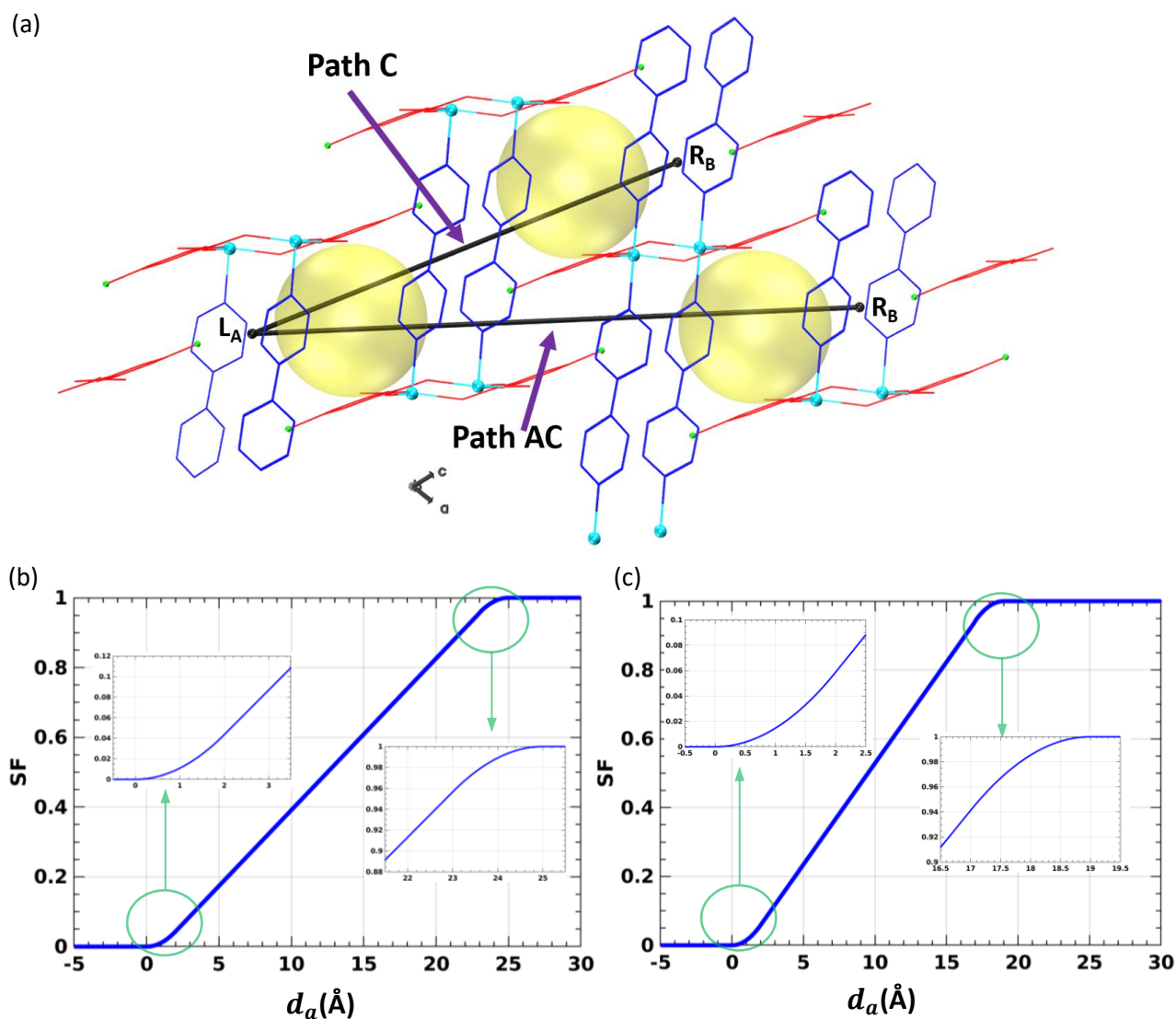


Figure S4: (a) Position of \mathbf{L}_A and \mathbf{R}_B in the CID-Me MOF to define switching function (SF) collective variable (CV) along Path AC (along ac axis) and Path C (along c axis). Variation of SF with d_a for (b) path AC and (c) path C; insets detail the variation near inflation points.

addition of bias between only two pores and avoids sampling of other pores, without the need to apply walls along the direction of CV. This SF uniquely defines the position of CO_2 molecule (with the help of d_a) between \mathbf{L}_A and \mathbf{R}_B , in the direction of pore channel. For the pores to the left of \mathbf{L}_A the SF has same value of 0 (as $d_a \leq 0$), therefore in WTM simulations all the positions of CO_2 in the left of \mathbf{L}_A are treated as the same and the corresponding bias will be the same as on \mathbf{L}_A . We chose \mathbf{L}_A at the left edge of pore A such that it has a little higher free energy compared to the pore but much lesser compared to

the height of free energy barrier. This discourages the transition of CO₂ to pores left of **L_A** in a periodic free-energy landscape (Figure S3 (b)). Similarly, for pores on the right of **L_B** (pore B) the SF has same value of 1 (as $d_a \geq |\vec{P}|$), therefore in metadynamics all the positions of CO₂ in the right of **L_B** are treated as the same and the corresponding bias will be same as on **L_B**, which discourages CO₂ transition to other pores in the right of **L_B**. Thus, this choice of SF as CV allows the addition of bias between only two pores and avoid sampling of other pores.

Here, we obtained the free-energy profile for CO₂ transition along path AC and path C. Details of paths are shown in Figure 4a. For path AC, the $|\vec{P}|$ is ~ 24.5 Å, therefore, for the construction of SF we used $y_{ca}=46.04348$, $y_{cb}= -45.0265$, $x_1 = 0$, $x_2 = 1$, $x_3 = 2$, $x_4 = 23$, $x_5 = 24$, and $x_6 = 25$. For path C, the $|\vec{P}|$ is ~ 18.8 Å, therefore, for construction of SF, we used $y_{ca}=34.05691$, $y_{cb}= -33.0271$, $x_1 = 0$, $x_2 = 1$, $x_3 = 2$, $x_4 = 17$, $x_5 = 18$, and $x_6 = 19$. Profile of SF with d_a along both paths are shown in Figure S4 b-c.

Although the switching function CV biases only the position of CO₂ between pores, however, due to presence of slow modes involved in the opening of gate(s), we had to use other distance CVs in combination with SF to obtain the state of free diffusion of CO₂ between pores. For the path AC, we used two distances between Meb groups (or gates) as additional CVs and for path C, we used the distance between methyl of two Meb groups as additional CV (details of distance CVs are given in Figure S15). Details of WTM simulation parameters are given in Table S4. In addition to applied bias on corresponding CV, lower walls potential with force constant 500 kcal/mol-Å² were applied on path C (AC) between the position of CO₂ molecule and gates towards path AC (C) to restrict its motion towards path AC (C).

Table S4: Details of WTM simulation parameters

Details	CV	Gaussian width	Initial gaussian height (kcal/mol)	Bias deposition rate	Bias factor
PY1 ring rotation	dihedral angle $\phi_{O-Zn-N-C}$	0.02 (radian)	0.4	500	20
PY2 ring rotation	dihedral angle $\phi_{O-Zn-N-C}$	0.02 (radian)	0.2	500	15
Path C: 1CV	SF	0.01	0.4	500	20
Path C: 2CVs	SF	0.01	0.3	200	15
	d _C	0.2 (Å)			
Path AC: 1CV	SF	0.01	0.2	500	20
Path AC: 3CV	SF	0.01	0.2	200	15
	d ₁	0.2 (Å)			
	d ₂	0.2 (Å)			

S1.7.4 Estimation of rates from the free energy profile

The free energy profile gives an estimate of the free-energy barrier height. The rate (k) of barrier crossing was obtained using the Eyring equation $k = \frac{k_B T}{h} e^{\frac{-\Delta F}{RT}}$ s⁻¹, where k_B is Boltzmann's constant, T is temperature, ΔF is the barrier height, and R is the universal gas constant. Inverse of the rate gives an estimate for the typical time to cross the barrier ($t = 1/k$ s). Barrier recrossing was not considered, for the sake of simplicity.

Section S2: Results

S2.1 Grand Canonical Monte Carlo (GCMC) Simulation Results

GCMC simulations provide the equilibrium adsorption uptake. To understand the energetics of CO₂ adsorption, we also calculated the heat of adsorption at very low uptake at 300 (and 195) K and found a value of -10.16 (and -11.59) kcal/mol which is close to the binding energy value of -10.9 kcal/mol, calculated using DFT for one CO₂ molecule (see main manuscript).

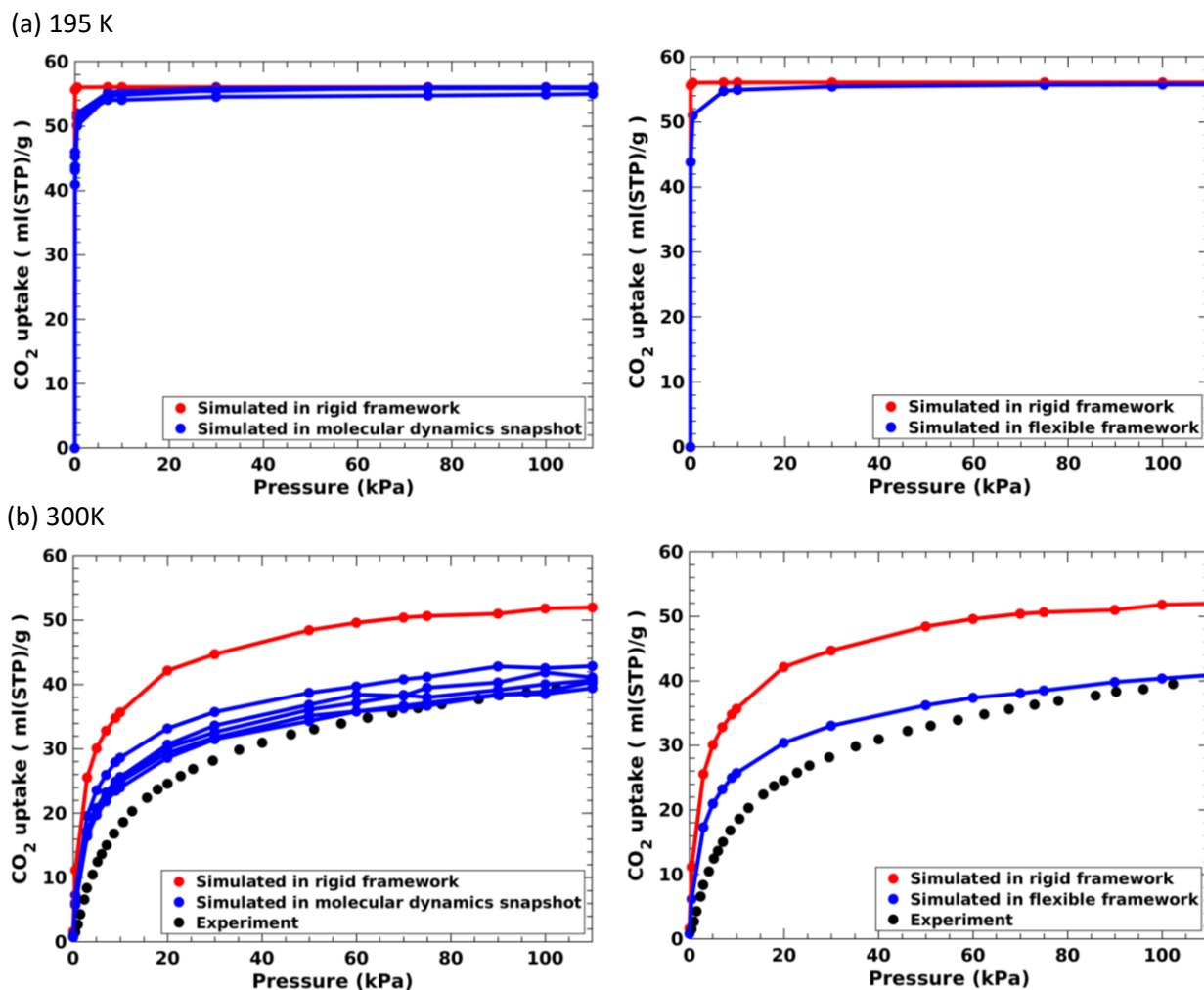


Figure S5: Simulated CO₂ adsorption isotherms in CID-Me MOF at (a) 195 K and (b) 300 K in the corresponding rigid experimental structures (red) at respective temperatures. The simulated CO₂ adsorption isotherms were also obtained in five snapshots of MOF structure (blue) taken from the molecular dynamics (MD) simulation trajectories (after 10 ns of MD run five snapshots were taken with a time gap of 5 ns). The simulated adsorption isotherm in flexible framework (left of (a) and (b)) was obtained using the average of the simulated adsorption isotherms in MD snapshots. Comparison with available experimental data¹³ (black) at 296 K is shown in (b).

S2.2 AIMD and MD Simulations Result

Comparison of AIMD and MD Simulations

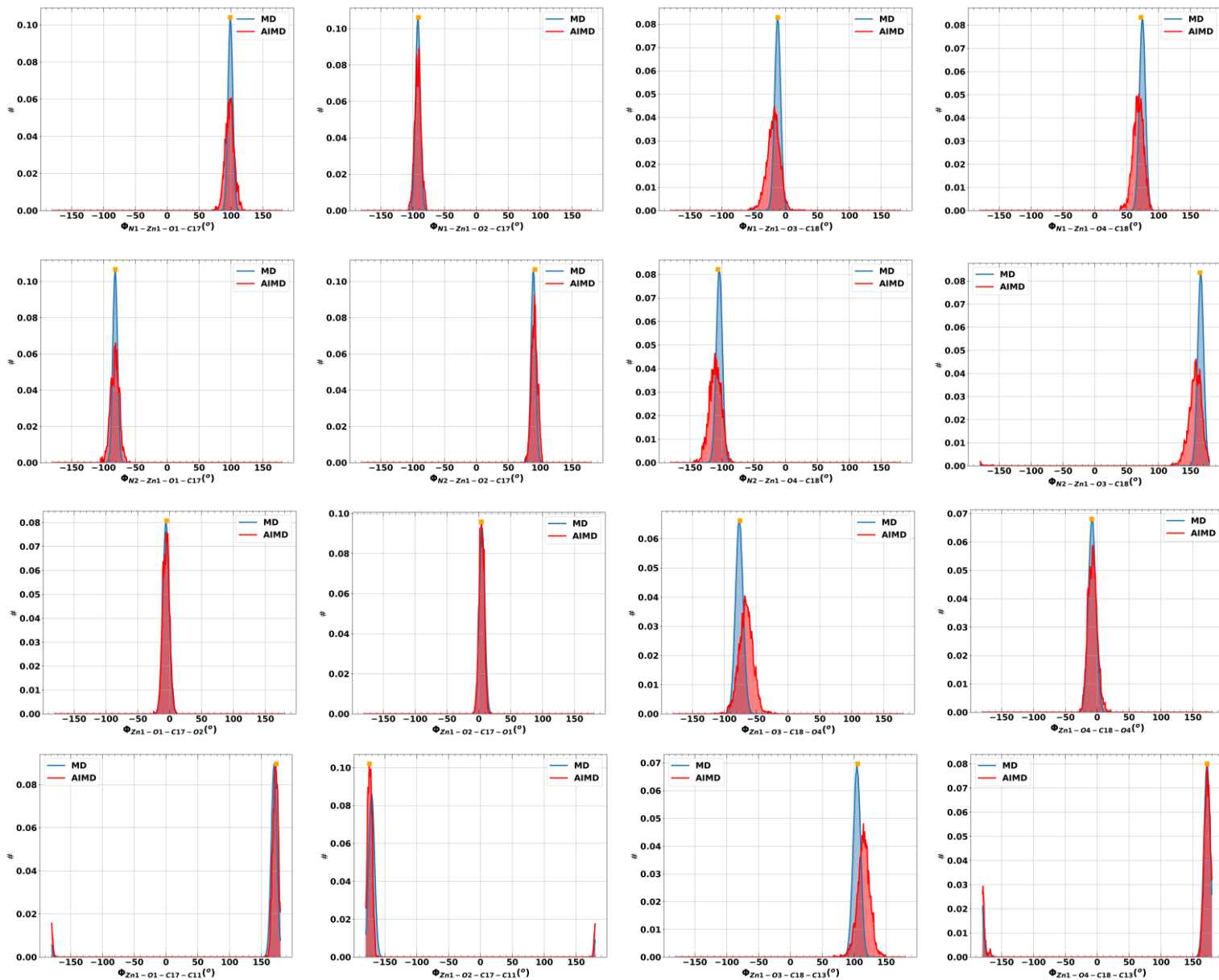


Figure S6: Distribution of proper torsional angles during 10 ps of AIMD (red) and 50 ns (blue) of MD simulation at 300 K and their comparison with torsional angle values (orange square) in the experimental structure.

Comparison of XRD Patterns between the Experimental Structure and MD Snapshots

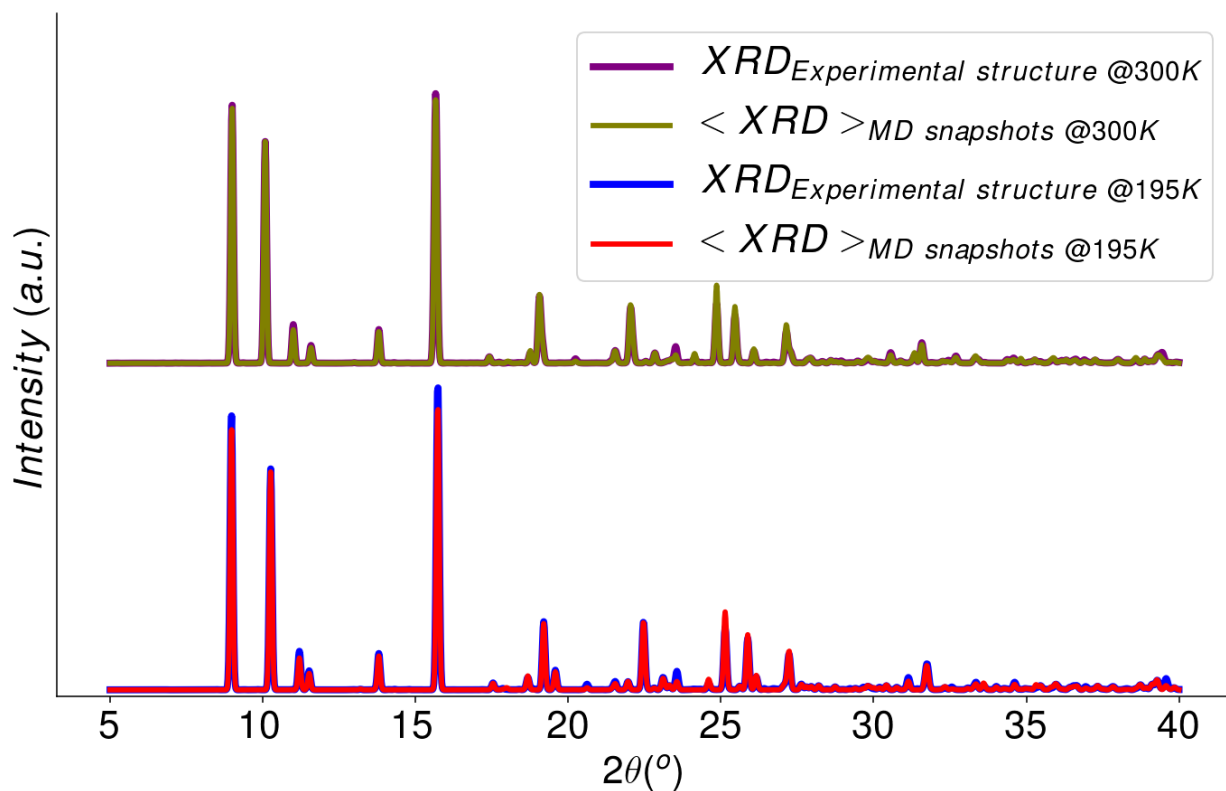


Figure S7: Comparison of simulated PXRD pattern (using Cu K α X-rays) of experimental structures at 195 and 300 K with the averages of PXRD pattern calculated 2000 different structures (or snapshots) generated using molecular dynamics (MD) simulations at the corresponding temperatures. An excellent comparison is observed between XRD patterns of experimental structure and its average over MD snapshots.

MD simulation results with 1 CO₂ molecule in a pore

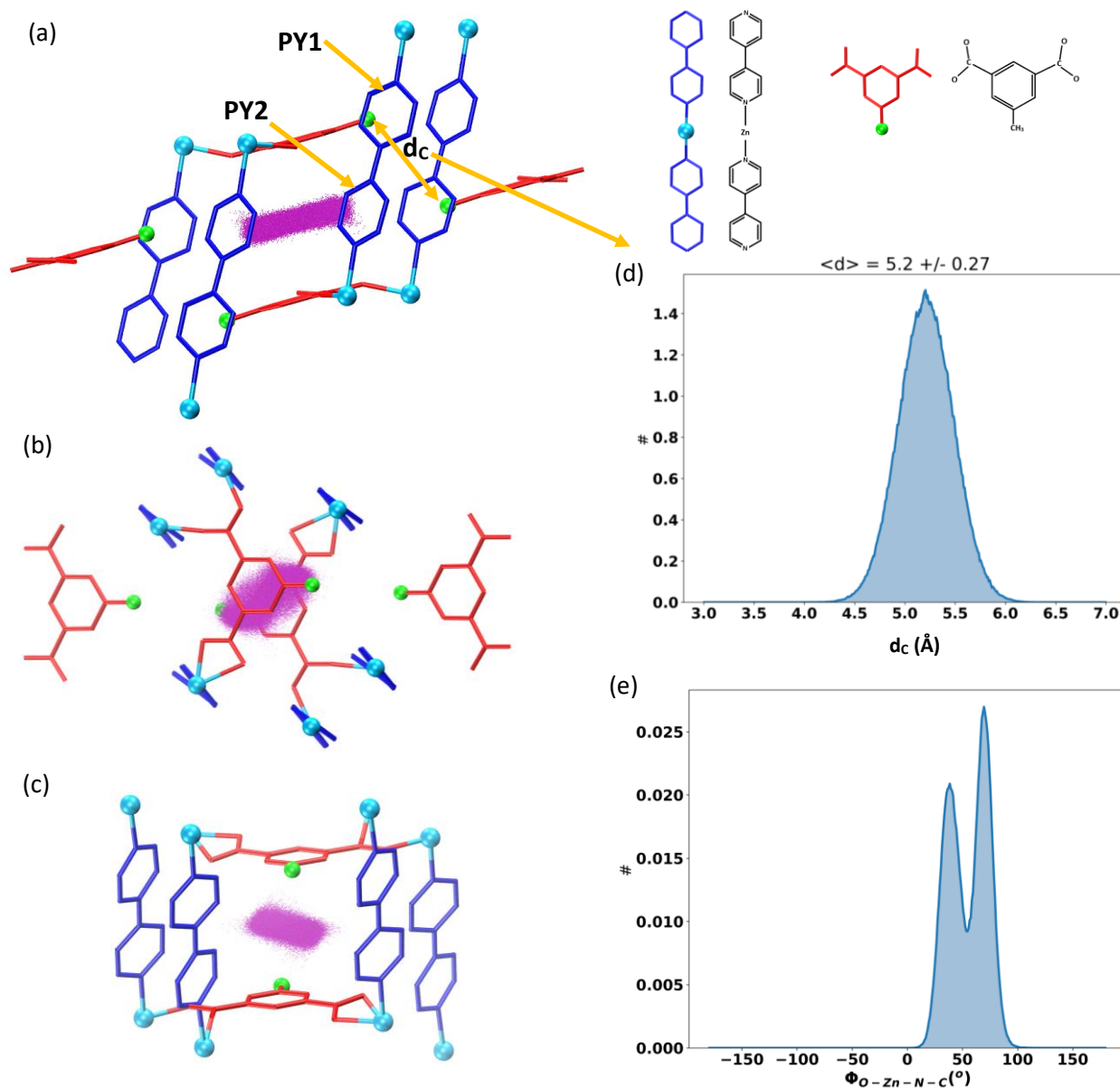


Figure S8: Trajectory of one CO₂ molecule in CID-Me MOF over an unbiased molecular dynamics (MD) simulation trajectory of 50 ns. The initial structure of MOF and the CO₂ trajectory are shown along three different views in (a), (b), and (c). Position of carbon of CO₂ is shown with purple dot (drawn every 0.5 ps). During the 50 ns simulation, CO₂ molecule remained in the same pore and did not show any transition to other pores. Normalized histograms of (d) distance between methyl (green) groups of two different Meb groups, and (e) dihedral angle $\phi_{O-Zn-N-C}$ of PY₂ (pyridine ring), during 50 ns MD simulation.

S2.3 WTM Simulations for PY Ring Rotation

Among both PY rings of a bpy linker, the PY₁ is sterically hindered to rotate, therefore we observed a very high free-energy barrier (> 28 kcal/mol) between two free energy minima of PY₁ ring rotation. The PY₂ ring is relatively free to rotate, and we observed 4 minima in a group of 2+2, where 2 adjacent minima have free energy barrier of ~ 1 kcal/mol and the free energy barrier between both groups is ~ 11.7 kcal/mol. These observations are in accordance with experimental ²H solid-state NMR findings, where only a static mode was found for sterically hindered PY₁, while the other free pyridine PY₂ showed two rotational modes (4-site and 2-site flips at 600 kHz (296 K)).¹³

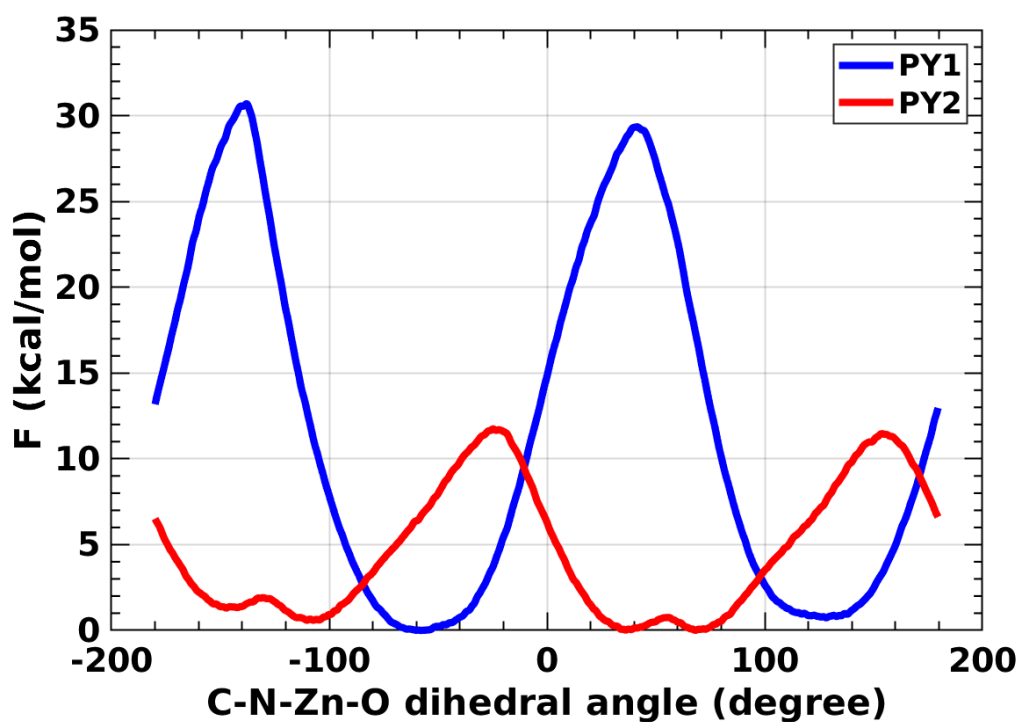


Figure S9: Free energy profile obtained using well-tempered metadynamics (WTM) simulations for the rotation of PY₁ and PY₂ pyridine rings at 300 K. The dihedral angle was used as the collective variable (CV) for the WTM simulations.

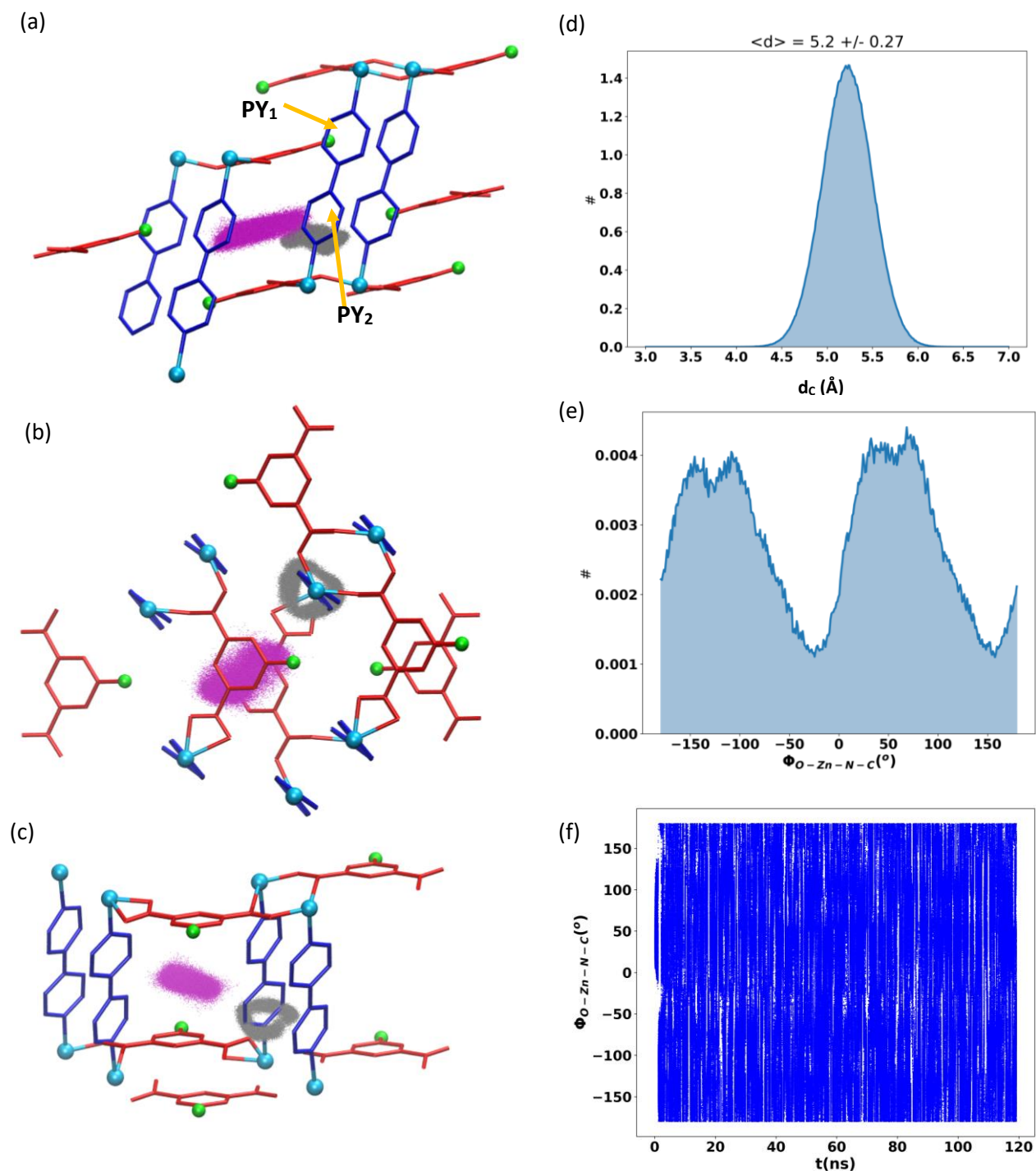


Figure S10: Trajectory of one CO₂ molecule motion and rotation of PY₂ ring in CID-Me MOF over WTM simulation of 120 ns. The structure of MOF and CO₂ trajectory are shown along three different views in (a), (b), and (c). Position of C of CO₂ is shown with purple dots and C (connected to N) of PY₂ ring is shown with gray dots (for 60000 MD snapshots). During the 120 ns simulation, PY₂ ring rotated many times, however, the CO₂ molecule remained in the same pore and did not show any transition to other pores. Histograms of (d_c) distance between methyl (green) groups of two different Meb groups, and (e) dihedral angle $\phi_{O-Zn-N-C}$ distribution of PY₂, during the 120 ns WTM simulation. (f) Variation of $\phi_{O-Zn-N-C}$ with time during the WTM simulation.

S2.4 WTM Simulations Results for CO₂ diffusion between pores.

S2.4.1 Only switching function (SF) as CV

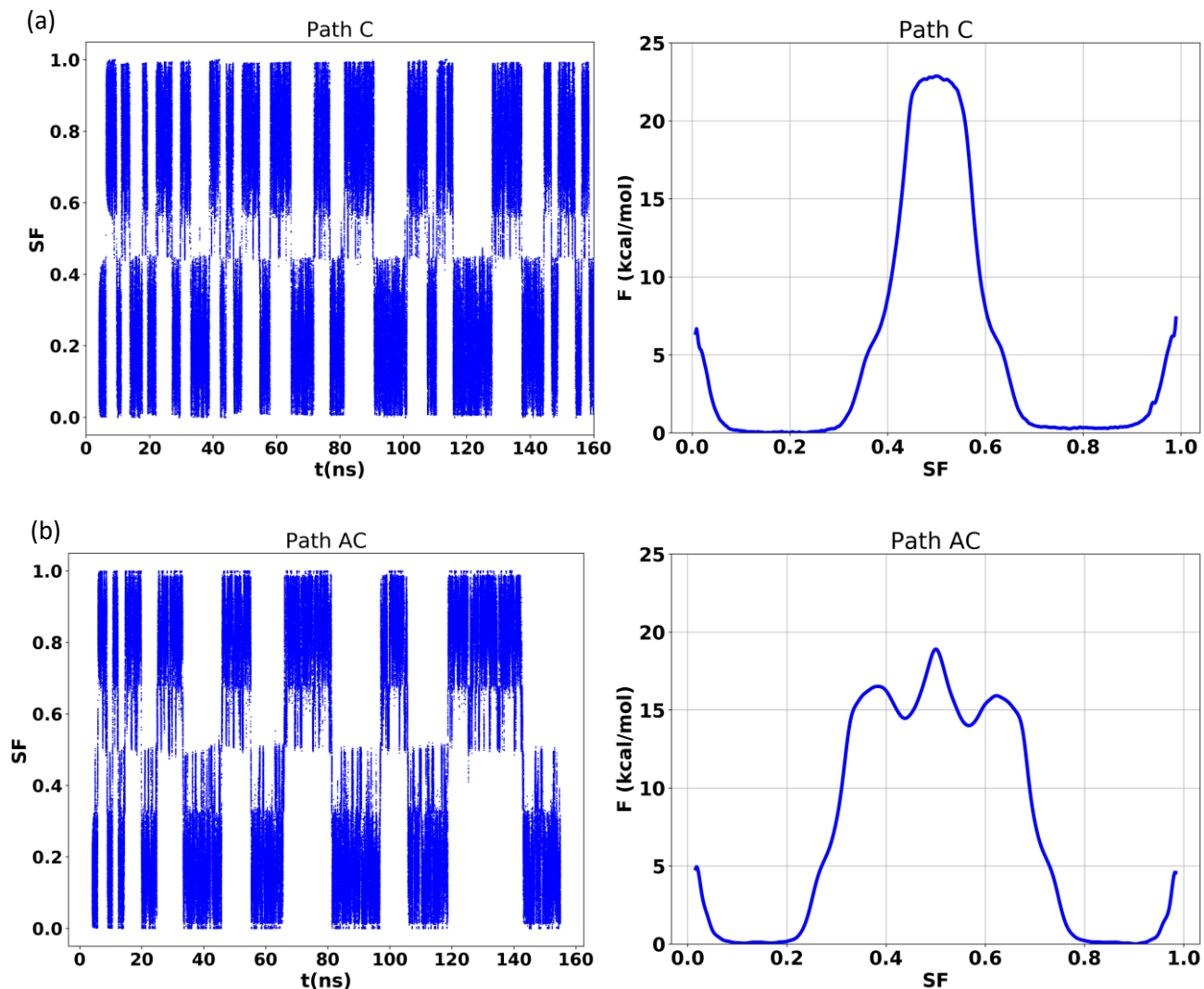


Figure S11: Results of well-tempered metadynamics (WTM) simulations where only SF (see Figure S4 for details) was used as collective variable and biased along the (a) path C and (b) path AC. Left: variation of SF with simulation time; right: estimate of free energy (by summing the deposited Gaussian kernels and scaling it with $\frac{\gamma}{1-\gamma}$ (γ is the bias factor)). A hysteresis is observed in SF with increasing time, which indicates the presence of other slow modes during the CO₂ transition between pores.

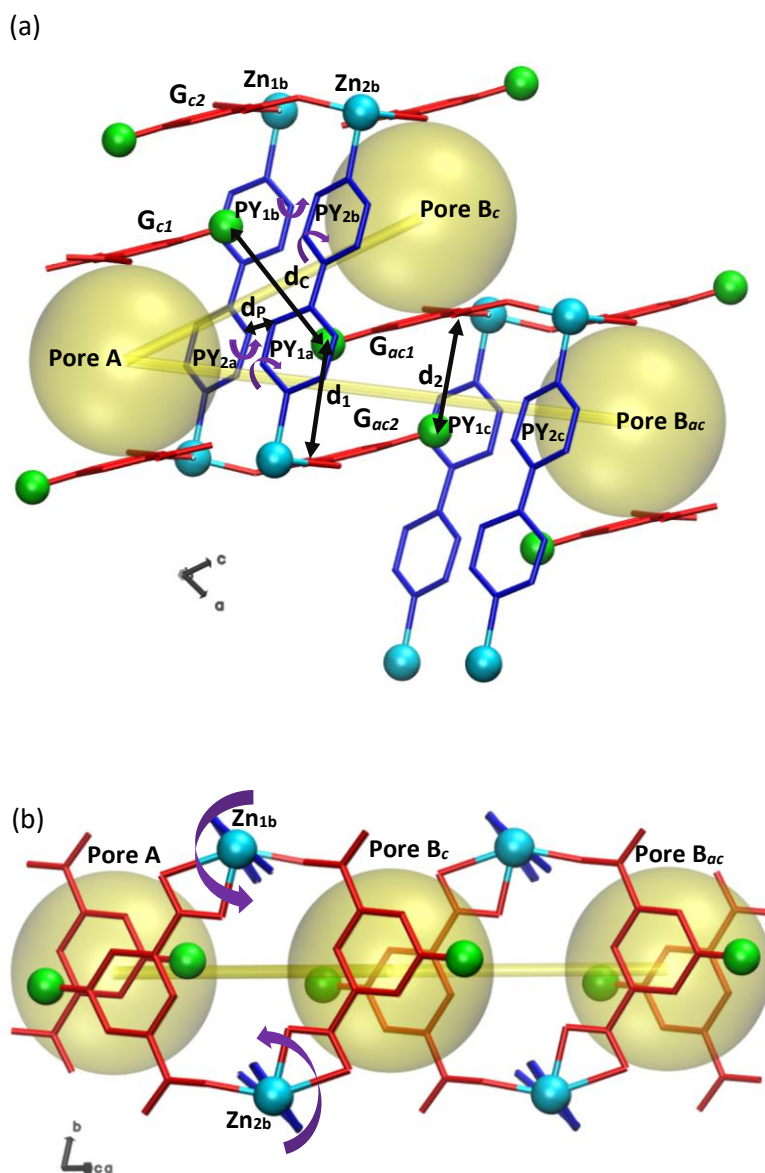


Figure S12: Location of pores (yellow sphere) relative to each other in CID-Me MOF from (a) side and (b) top view. Transition of a CO₂ molecule can take place from pore A to either pore B_c (path C along *c* axis) or pore B_{ac} (path AC along *ac* axis). The size of pore window along either of the path is smaller than the kinetic diameter of CO₂ molecule (3.3 Å). The transition of CO₂ molecule along path C is facilitated by rotation of four pyridine rings (PY) and opening of Meb (in red) gates (G_x). The direction of rotation of PY rings (for opening of pore window) are shown with purple arrow. Size of pore window along path C can be characterized using the distance between two Py rings (*d_P*) and distance between methyl of Meb gates (*d_C*). The full rotation of PY_{1x} is sterically hindered due to methyl (green) of Meb group while PY_{2x} has no steric hinderance from methyl of Meb group. Along path AC, the transition of CO₂ is facilitated by opening of two Meb gates G_{ac1} and G_{ac2}, quantified by distances *d₁* and *d₂*, respectively.

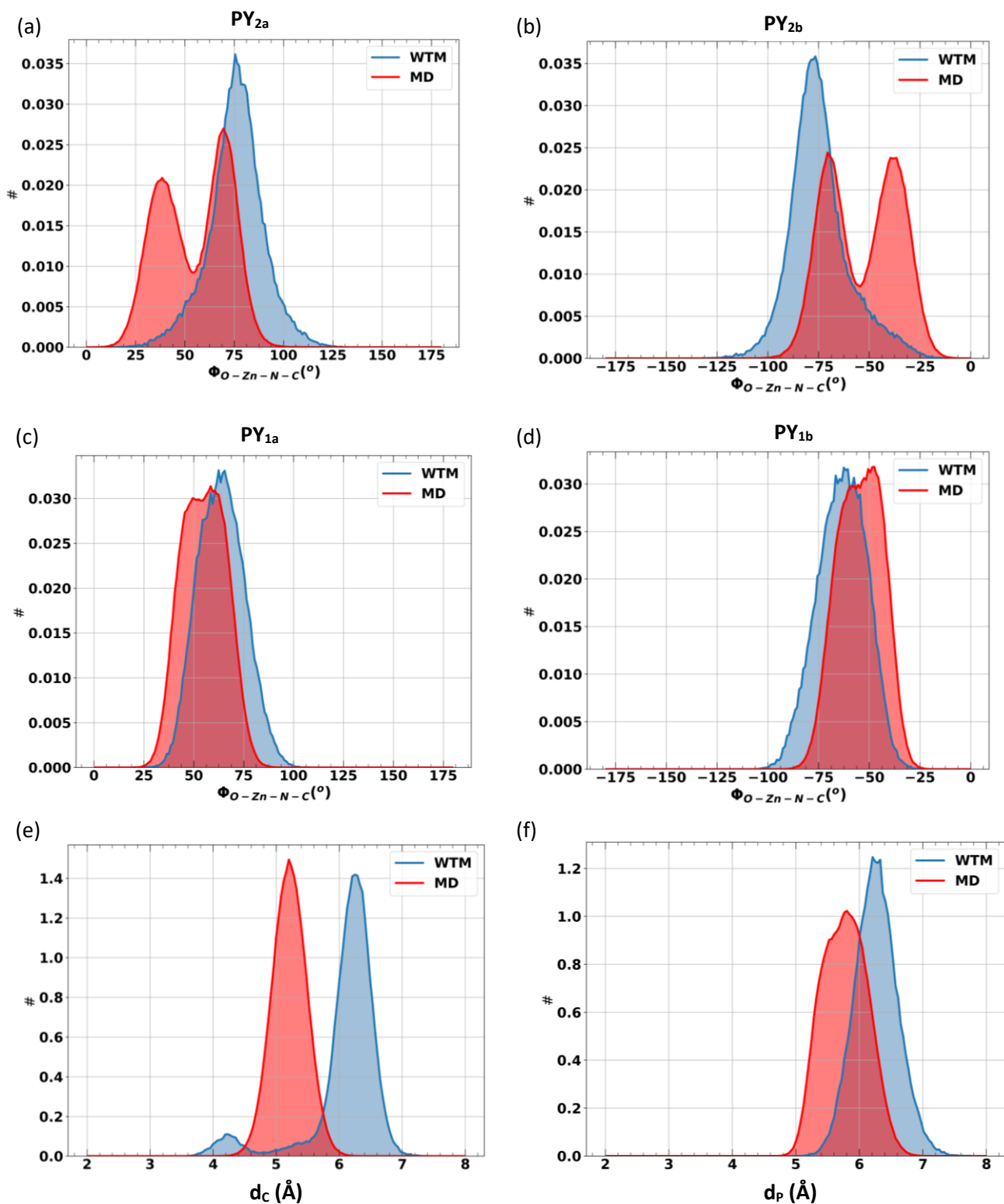


Figure S13: Distribution of proper torsional angles $\phi_{O-Zn-N-C}$ corresponding to the rotation of (a) PY_{2a}, (b) PY_{2b}, (c) PY_{1a}, and (d) PY_{1b} linkers, and distances (e) d_c and (f) d_p during an unbiased 50 ns MD simulation (in the presence of one CO₂ molecule in the pore) and in the WTM simulations with biased SF (see Figure S3-4 for details) over position of CO₂ along path C. The distributions corresponding to WTM are shown only for the transition state region (i.e., $0.44 < SF < 0.56$).

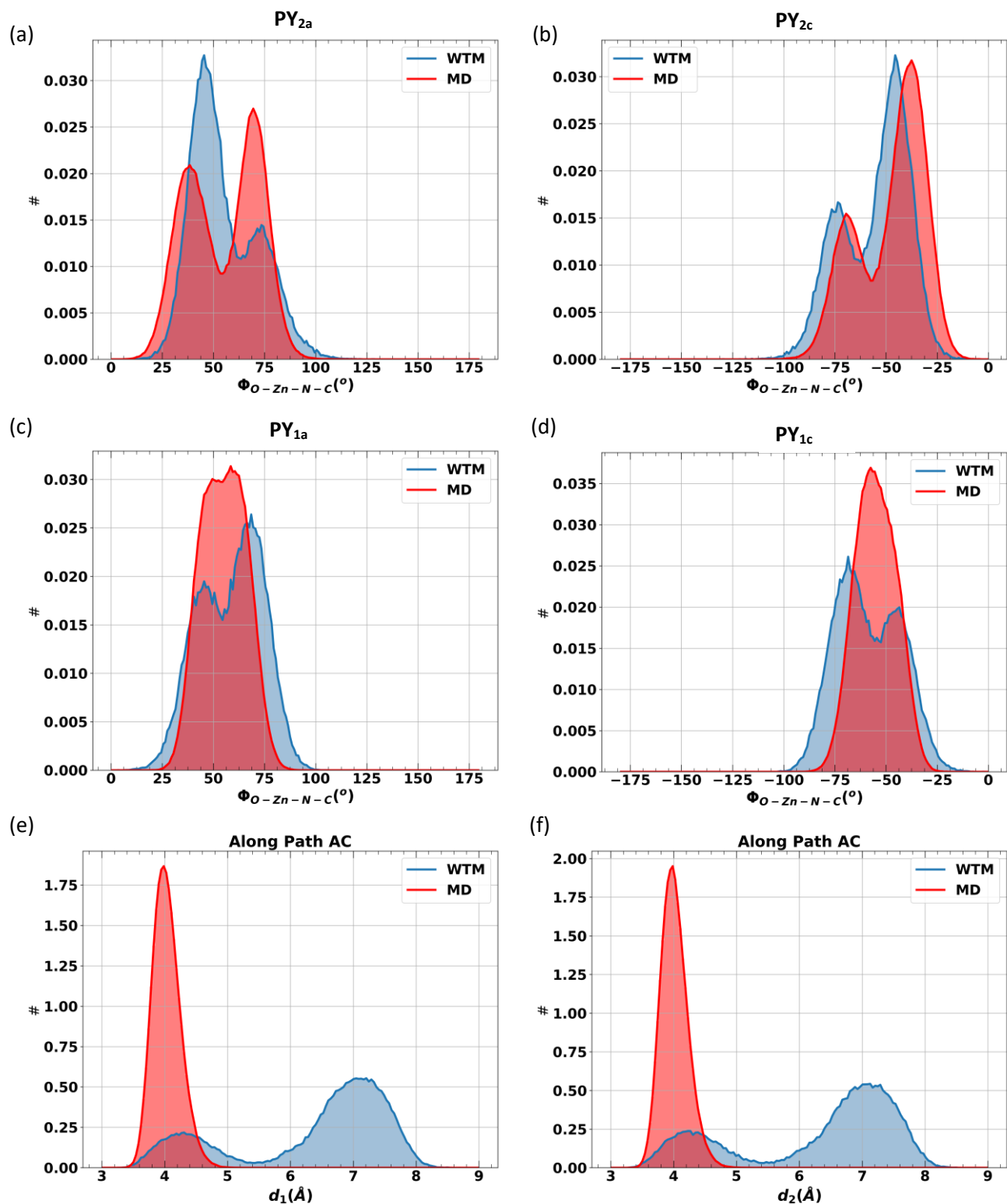


Figure S14: Distribution of proper torsional angles $\phi_{O-Zn-N-C}$ corresponding to rotation of (a) PY_{2a}, (b) PY_{2c}, (c) PY_{1a}, and (d) PY_{1c} linkers, and distances (e) d_1 and (f) d_2 during unbiased 50 ns MD simulation (in the presence of one CO₂ molecule in the pore) and in the WTM simulations with biased SF (see Figure S3-4 for details) over position of CO₂ along the path AC. The distributions corresponding to WTM are shown only for the transition state region ($0.32 < SF < 0.56$ for d_1 , PY_{2a}, and PY_{1a}; $0.44 < SF < 0.68$ for d_2 , PY_{2c}, and PY_{1c}).

S2.4.2 SF and atomic distances as CV

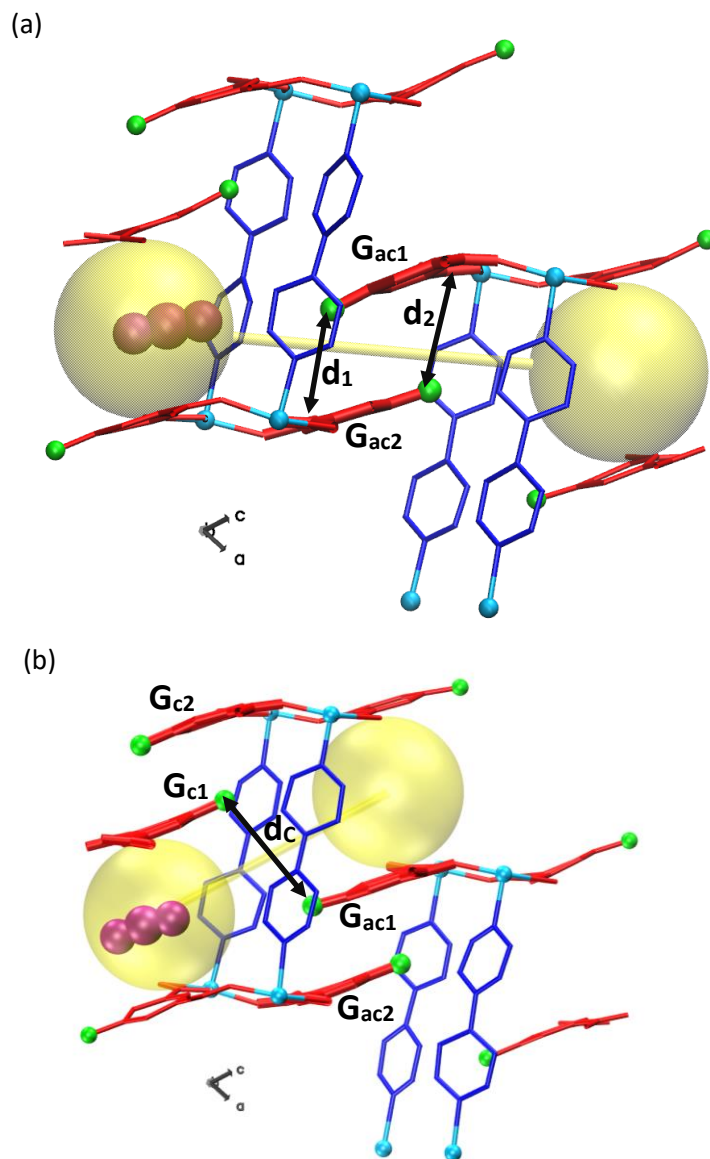


Figure S15: Distance CVs for path (a) AC and (b) C. For path AC, two similar distance CVs d_1 and d_2 were used those control the opening/closing of Meb gates G_{ac1} and G_{ac2} . For path C, one distance CV d_c was used that controls the relative distance between gates G_{c1} and G_{ac1} . The d_c explicitly controls relative motion of gates G_{c1} and G_{ac1} and implicitly affect the motion of gates G_{c2} and G_{ac2} .

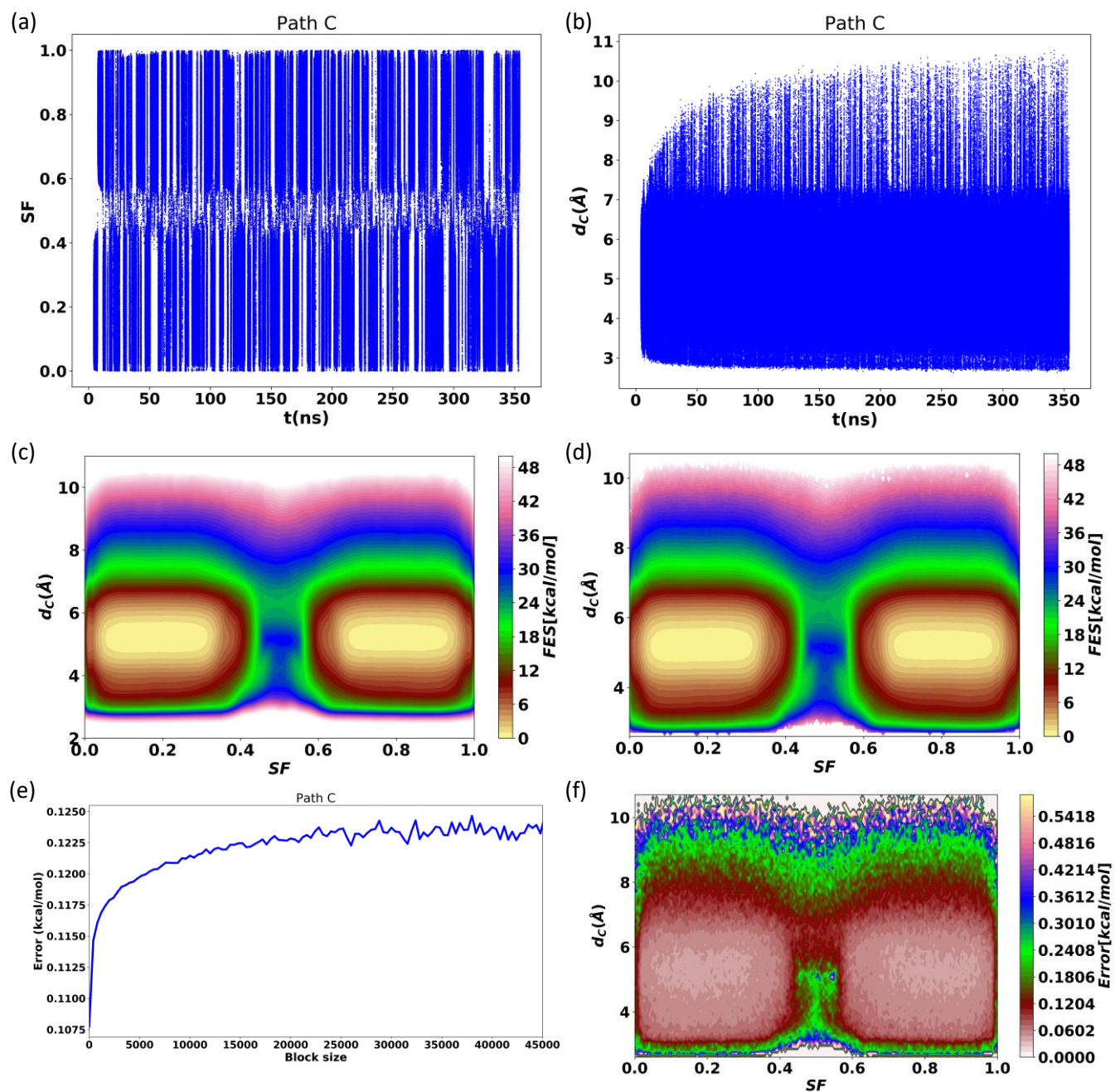


Figure S16: Results of WTM simulation where both SF (along path C) and d_c were biased to estimate the free energy surface. Variation of (a) SF and (b) d_c with time during WTM simulation. Estimated free energy surface (FES) by (c) summing the deposited hills and (d) re-weighting with block averaging. (e) Variation of cumulative error with block size and (f) error as a function of CV. Maximum error of 0.12 kcal/mol is observed along the minimum free energy path.

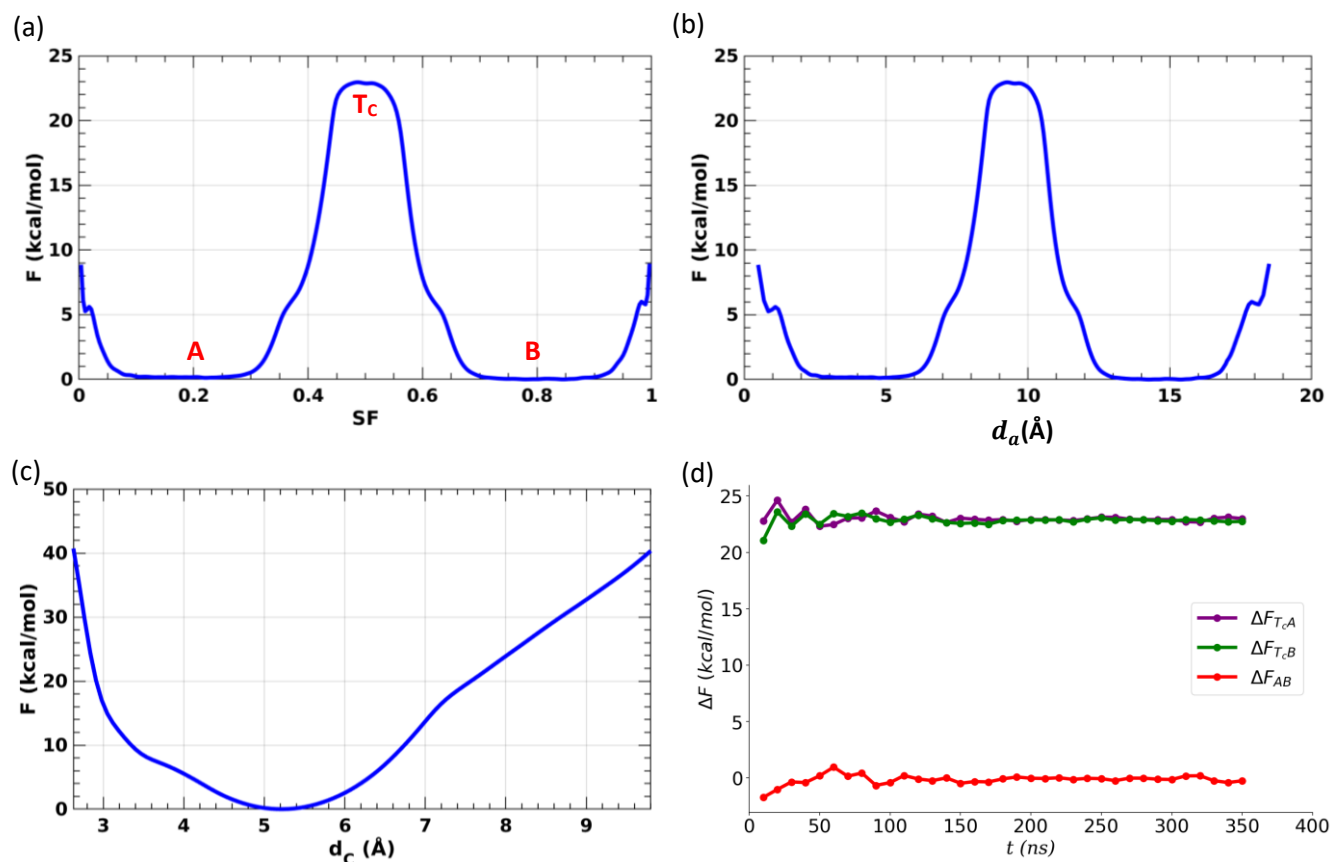


Figure S17: Integrated Free energy profile ($F(SF) = -k_B T \ln \int dd_c e^{F(SF, d_c)}$), in WTM simulation where both SF (along path C) and d_c were biased, with respect to (a) SF along path C, (b) d_a (defined in Figure S3) along path C, and (c) d_c . In (a), A and B represent stable states in the pore and T_c represents transition state. (c) The free energy difference between different states given in (a) during 350 ns WTM simulation.

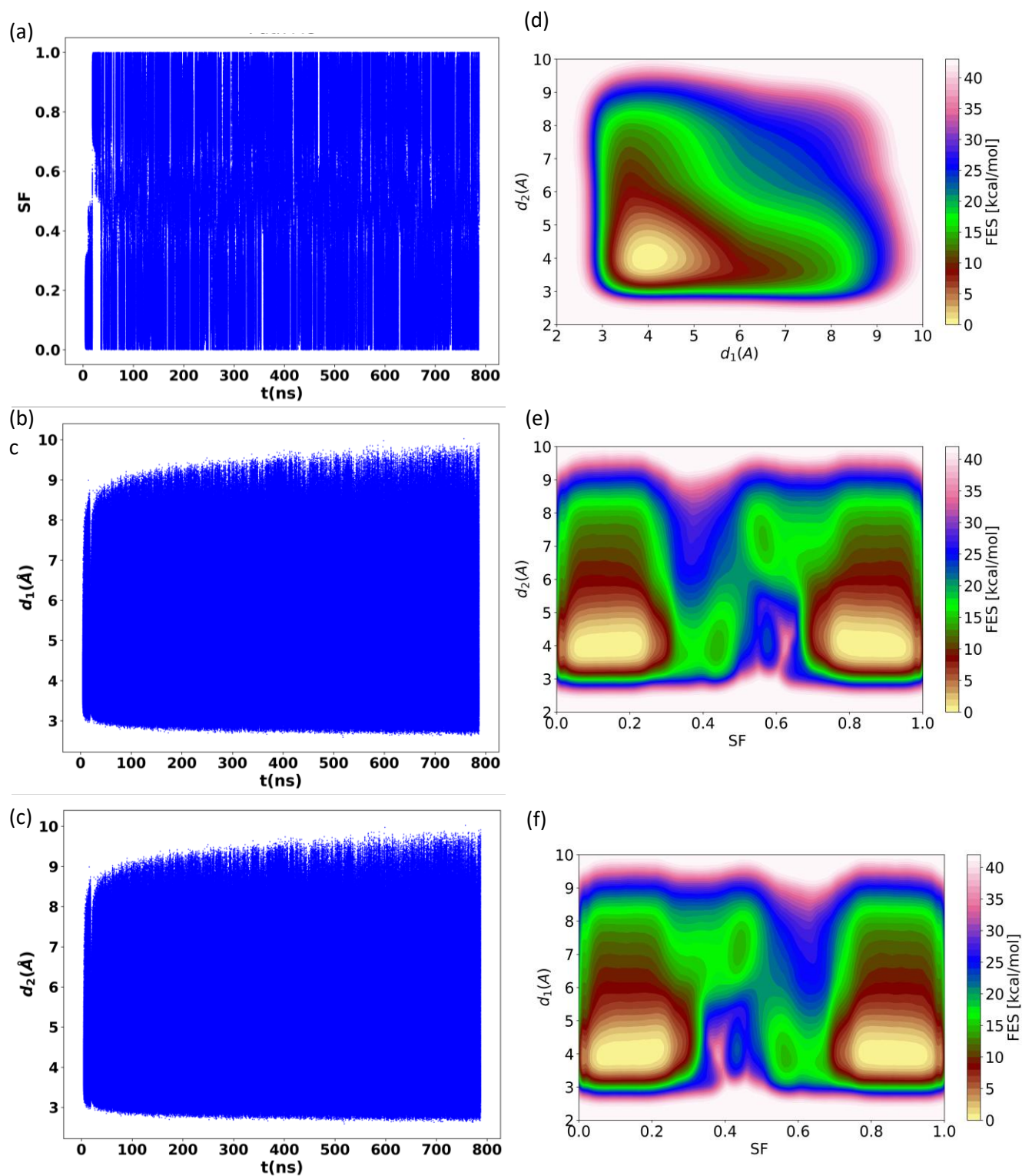


Figure S18: Results of WTM simulation where SF (along path AC), d_1 , and d_2 were biased to estimate free energy surface. (a)-(c) Variation of CVs with time during WTM simulation. (d)-(f) Estimated 2D FES (by integrating FES over third CV as $F(x_1, x_2) = -k_B T \ln \int dx_3 e^{F(x_1, x_2, x_3)}$) using summation of the deposited hills.

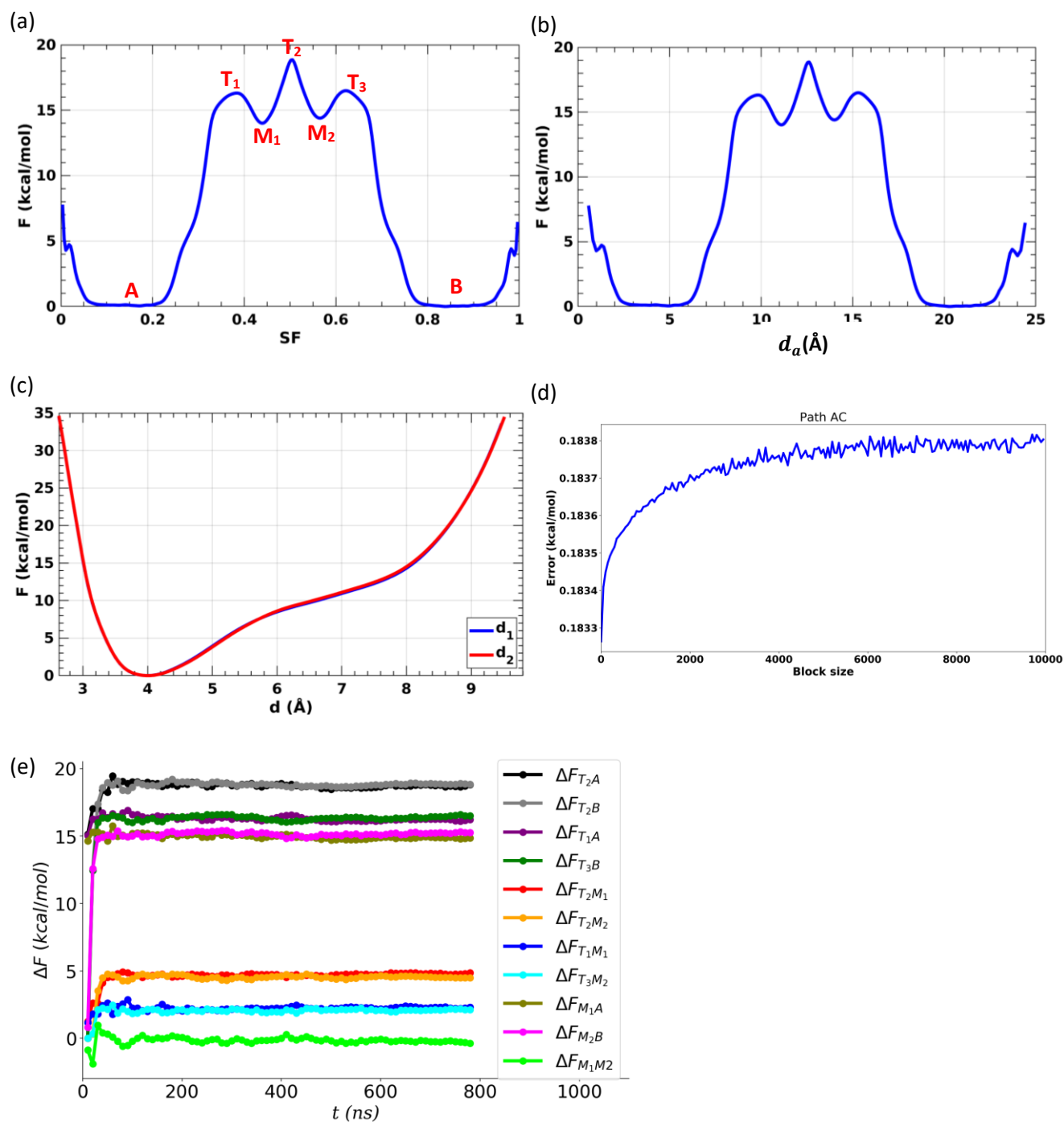


Figure S19: (a)-(c) Free energy profile as a function of one CV (using WTM simulation where SF (along path AC)), d_1 , and d_2 were biased). These profiles were obtained by integrating FES over other two CV's as $F(x_1) = -k_B T \ln \int dx_2 dx_3 e^{F(x_1, x_2, x_3)}$. (d) Variation of cumulative error with the block size. (e) The free energy difference between different states given in (a) during 800 ns WTM simulation.

Section S3: Effect of Free Energy Barrier and Temperature on HAHT

To obtain a general understanding about the effect of height of free energy barrier (ΔF) for the diffusion of a gas molecule between neighboring pores and temperature (T), on kinetically governed HAHT (high adsorption at high temperature) phenomena, we used the Eyring equation ($k = \frac{k_B T}{h} e^{\frac{-\Delta F}{RT}}$ s⁻¹). This equation gives an estimate of rate (k) and the corresponding time ($t_p = 1/k$ s) for a gas molecule to jump from one pore to neighboring pores. For the sake of simplicity, we neglect barrier recrossing. In Figure S20a, each line shows the values of ΔF and T for a fixed value of t_p (e.g. green line corresponds to $t_p = 0.1$ s). This indicates that, if in a porous framework X (with a free energy barrier ΔF_X for transition of a gas molecule between pores) a gas molecule takes t_p time (at temperature T) for transition between pores, then in another framework Y (with $\Delta F_Y > \Delta F_X$) to achieve the same t_p , the temperature needs to be increased. In Figure S20a, the points right (and left) to a line represents fast (and slow) pore diffusion time compared to points on the line.

The filling of pores of a porous crystalline material depends on many parameters including the size of particle, shape of particle, size and dimensionality of the pores, size of pore channels, crystalline defects, temperature, pressure, interaction of gas molecules with the material, and free energy barrier for the diffusion of gas molecules inside a pore and between pores. Filling of a spherical particle under the gas pressure at a given temperature can be quantified using the Crank theory.^{27,28} Here, we used a simplified model to relate the pore diffusion time of a gas molecule to the filling of a crystal particle by the gas. Let us consider a crystalline porous framework where distance between neighboring pores is d Å and a gas molecule takes t_p time to jump between pores (i.e., covering the distance d Å in the framework). Also, we assume that there is no effect of temperature and pressure (or loading) on the gas diffusivity (and free energy barrier). Further, let us consider a spherical single crystallite particle of this porous framework of radius r_c which is in contact with gas molecules (Figure S20b). Therefore, to cover r_f ($r_f = r_c - r_e$) radial distance towards the particle center, a gas molecule takes $t_f = t_p r_f / d$ time (assuming gas molecules enters the surface of particle and only hop radially towards the center of particle without recrossing). Since, the full surface of spherical particle is in contact with the gas, therefore, in t_c time, the percentage of particle filled with gas molecules is $100(r_c^3 - r_e^3)/r_c^3$.

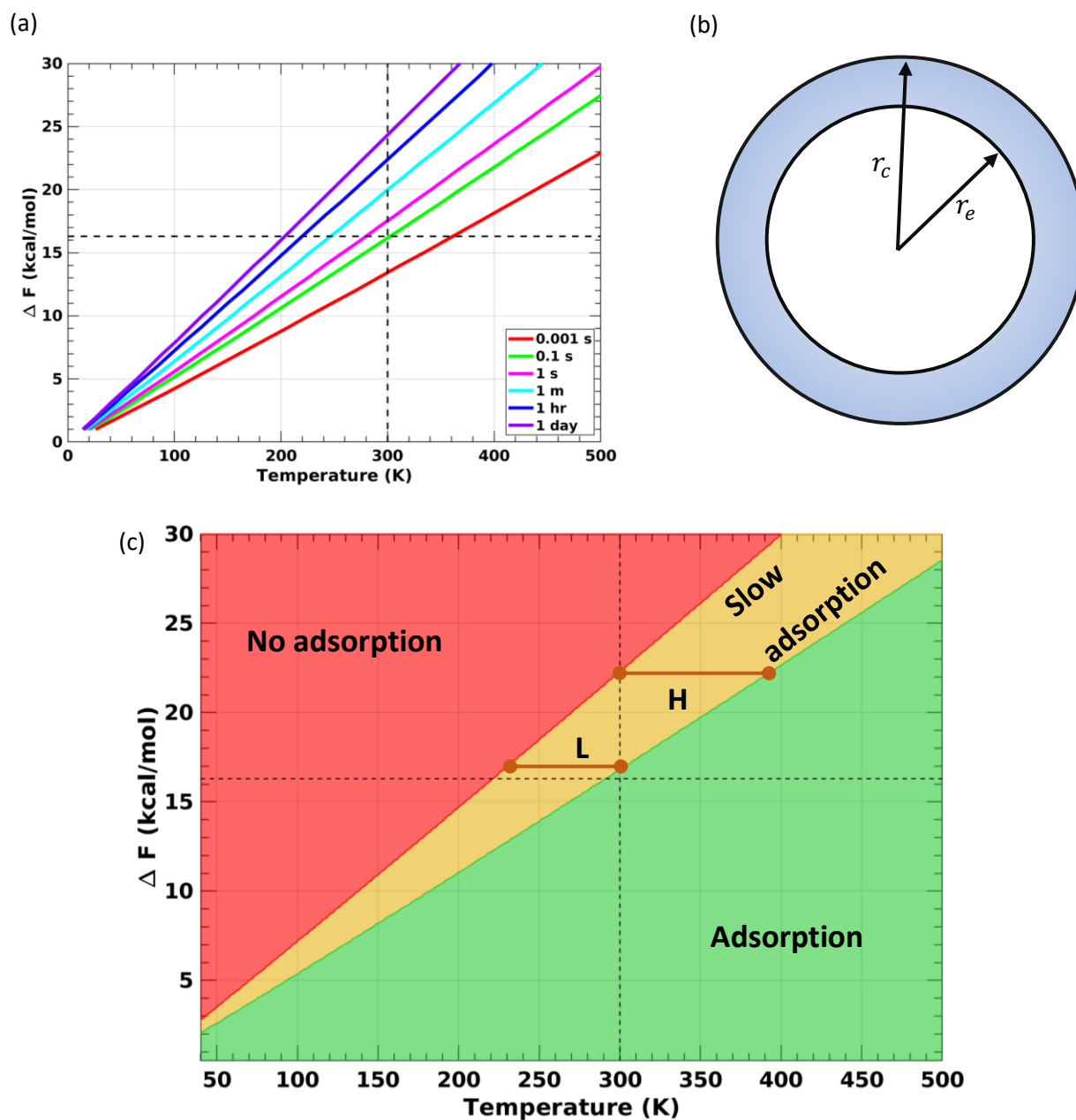


Figure S20: (a) Values of free energy barrier ΔF and temperature resulting in same time t_p (shown by each line) for crossing of the free energy barrier. (b) Simple model representing filling of a spherical crystallite particle of radius r_c . The filled portion of particle is shown in blue shade and empty portion (radius r_e) is shown in white. (c) Values of free energy barrier and temperature for the states of ‘no adsorption’ (red; $t_p > 3000$ s), ‘adsorption’ (green; $t_p < 0.3$ s), and ‘slow adsorption’ (yellow; $0.3 < t_p < 3000$). See text of section S3 for details. Horizontal dashed line is for $\Delta F=16.3$ kcal/mol and reveals adsorption above 291 K and no adsorption below 221 K. Vertical dashed line is for temperature 300 K and reveals adsorption and no adsorption for ΔF above 22.3 kcal/mol and below 16.9 kcal/mol, respectively. The line L represents value of free energy barrier below which state of adsorption can be observed at 300 K and guides to value of temperature (~ 230 K) below which state of no adsorption can be observed. Similarly, the line H represents value of free energy barrier above which state of no adsorption can be observed at 300 K and guides to value of temperature (~ 390 K) above which state of adsorption can be observed.

We define the state of ‘no adsorption’, if the % filling of the crystallite is $\leq 1\%$ during an adsorption experiment running for a day (~ 24 hr). For a spherical particle of radius $r_c = 10 \mu\text{m}$ (or 10^5 \AA), the r_f of 300 \AA corresponds to the pore filling of $\sim 1\%$. Considering $d \sim 10 \text{ \AA}$ and $t_f = 86400 \text{ s}$ (or 24 hr), the $t_p (=t_f d/r_c)$ results in 2880 s (or 48 min). Therefore, here we consider state of ‘no adsorption’ when $t_p \sim 50 \text{ min}$ (i.e., when gas molecule typically takes around 50 min to jump from one pore to another). Similarly, we considered the state of ‘adsorption’ to be present when $t_p \sim 0.3 \text{ sec}$ (the gas molecule can cover $r_c = 10^5 \text{ \AA}$ in an hour). The combination of ΔF and T values for the states of ‘adsorption’ and ‘no adsorption’ defined here is shown in Figure S20c. The intermediate region can be considered as the state of ‘slow adsorption’.

Figure S20c answers two key questions: 1) for a given free energy barrier, what are the range of temperatures for which states of ‘adsorption’ and ‘no adsorption’ can be achieved, and 2) at a given temperature what could be values of free energy barrier to achieve states of ‘adsorption’ and ‘no adsorption’? The first question can be answered by traversing horizontally in Figure S20c. For a temperature of 300 K , the state of ‘no adsorption’ is observed if the free energy barrier is above 22.3 kcal/mol and the state of ‘adsorption’ is observed if the free energy barrier is below 16.9 kcal/mol . Similarly, for a free energy barrier of 16.3 kcal/mol (corresponding to CO_2 diffusion between pores in CID-Me MOF, as revealed by WTM calculations) the state of ‘no adsorption’ remains below 221 K and state of ‘adsorption’ can be observed after 291 K . This free energy barrier needs to be crossed for both adsorption and desorption processes. Interestingly, in the experimental study¹³ of CID-Me MOF, no CO_2 desorption was observed below 223 K which is in good agreement with our analysis showing no adsorption (and desorption) near 221 K .

In the above discussion, we simplified the effect of free energy barrier and temperature to achieve states of ‘adsorption’ and ‘no adsorption’ using a simple model, assuming no change in gas diffusivity with loading and temperature. Adsorption in realistic condition depends on the experimental shape and size of particles, distance between pores, pressure, temperature, and loading dependent diffusivity. This caveat should be applied while using this simplified model.

Section S4: References

- (1) Vandevondele, J.; Krack, M.; Mohamed, F.; Parrinello, M.; Chassaing, T.; Hutter, J. Quickstep: Fast and Accurate Density Functional Calculations Using a Mixed Gaussian and Plane Waves Approach. *Comput. Phys. Commun.* **2005**, *167* (2), 103–128.
- (2) Kühne, T. D.; Iannuzzi, M.; Del Ben, M.; Rybkin, V. V.; Seewald, P.; Stein, F.; Laino, T.; Khaliullin, R. Z.; Schütt, O.; Schiffmann, F.; et al. CP2K: An Electronic Structure and Molecular Dynamics Software Package -Quickstep: Efficient and Accurate Electronic Structure Calculations. *J. Chem. Phys.* **2020**, *152* (19), 194103.
- (3) Goedecker, S.; Teter, M. Separable Dual-Space Gaussian Pseudopotentials. *Phys. Rev. B - Condens. Matter Mater. Phys.* **1996**, *54* (3), 1703–1710.
- (4) Perdew, J. P.; Burke, K.; Ernzerhof, M. Generalized Gradient Approximation Made Simple. *Phys. Rev. Lett.* **1996**, *77* (18), 3865–3868.
- (5) Grimme, S.; Antony, J.; Ehrlich, S.; Krieg, H. A Consistent and Accurate *Ab Initio* Parametrization of Density Functional Dispersion Correction (DFT-D) for the 94 Elements H-Pu. *J. Chem. Phys.* **2010**, *132* (15), 154104.
- (6) Bussi, G.; Donadio, D.; Parrinello, M. Canonical Sampling through Velocity Rescaling. *J. Chem. Phys.* **2007**, *126* (1), 014101.
- (7) Rappe, A. K.; Casewit, C. J.; Colwell, K. S.; Goddard, W. A.; Skiff, W. M. UFF, a Full Periodic Table Force Field for Molecular Mechanics and Molecular Dynamics Simulations. *J. Am. Chem. Soc.* **1992**, *114* (25), 10024–10035.
- (8) Dubbeldam, D.; Calero, S.; Ellis, D. E.; Snurr, R. Q. RASPA: Molecular Simulation Software for Adsorption and Diffusion in Flexible Nanoporous Materials. *Mol. Simul.* **2016**, *42* (2), 81–101.
- (9) Potoff, J. J.; Siepmann, J. I. Vapor–Liquid Equilibria of Mixtures Containing Alkanes, Carbon Dioxide, and Nitrogen. *AIChE J.* **2001**, *47* (7), 1676–1682.
- (10) Anderson, K. E.; Mielke, S. L.; Ilja, J. S.; Truhlar, D. G. Bond Angle Distributions of Carbon Dioxide in the Gas, Supercritical, and Solid Phases. *J. Phys. Chem. A* **2009**, *113* (10), 2053–2059.

- (11) Plimpton, S. Fast Parallel Algorithms for Short-Range Molecular Dynamics. *J. Comput. Phys.* **1995**, *117* (1), 1–19.
- (12) Martyna, G. J.; Klein, M. L.; Tuckerman, M. Nosé–Hoover Chains: The Canonical Ensemble via Continuous Dynamics. *J. Chem. Phys.* **1998**, *97* (4), 2635.
- (13) Inukai, M.; Tamura, M.; Horike, S.; Higuchi, M.; Kitagawa, S.; Nakamura, K. Storage of CO₂ into Porous Coordination Polymer Controlled by Molecular Rotor Dynamics. *Angew. Chemie Int. Ed.* **2018**, *57* (28), 8687–8690.
- (14) Willems, T. F.; Rycroft, C. H.; Kazi, M.; Meza, J. C.; Haranczyk, M. Algorithms and Tools for High-Throughput Geometry-Based Analysis of Crystalline Porous Materials. *Microporous Mesoporous Mater.* **2012**, *149* (1), 134–141.
- (15) Van Heerden, D. P.; Barbour, L. J. Guest-Occupiable Space in the Crystalline Solid State: A Simple Rule-of-Thumb for Predicting Occupancy. *Chem. Soc. Rev.* **2021**, *50* (2), 735–749.
- (16) Allen, M. P.; Tildesley, D. J. *Computer Simulation of Liquids*; Clarendon Press: Oxford, 1996.
- (17) Rappe, A. K.; Goddard, W. A. Charge Equilibration for Molecular Dynamics Simulations. *J. Phys. Chem.* **1991**, *95* (8), 3358–3363.
- (18) Sharma, A.; Huang, R.; Malani, A.; Babarao, R. Computational Materials Chemistry for Carbon Capture Using Porous Materials. *J. Phys. D. Appl. Phys.* **2017**, *50* (46), 463002.
- (19) Beerdsen, E.; Smit, B.; Dubbeldam, D. Molecular Simulation of Loading Dependent Slow Diffusion in Confined Systems. *Phys. Rev. Lett.* **2004**, *93* (24), 248301.
- (20) Dubbeldam, D.; Beerdsen, E.; Vlugt, T. J. H.; Smit, B. Molecular Simulation of Loading-Dependent Diffusion in Nanoporous Materials Using Extended Dynamically Corrected Transition State Theory. *J. Chem. Phys.* **2005**, *122* (22), 224712.
- (21) Jee, S. E.; Sholl, D. S. Carbon Dioxide and Methane Transport in DDR Zeolite: Insights from Molecular Simulations into Carbon Dioxide Separations in Small Pore Zeolites. *J. Am. Chem. Soc.* **2009**, *131* (22), 7896–7904.
- (22) Camp, J. S.; Sholl, D. S. Transition State Theory Methods To Measure Diffusion in Flexible Nanoporous Materials: Application to a Porous Organic Cage Crystal. *J. Phys. Chem. C* **2016**, *120* (2), 1110–1120.

- (23) Laio, A.; Parrinello, M. Escaping Free-Energy Minima. *Proc. Natl. Acad. Sci. U. S. A.* **2002**, *99* (20), 12562–12566.
- (24) Barducci, A.; Bussi, G.; Parrinello, M. Well-Tempered Metadynamics: A Smoothly Converging and Tunable Free-Energy Method. *Phys. Rev. Lett.* **2008**, *100* (2), 020603.
- (25) Bonomi, M.; Bussi, G.; Camilloni, C.; Tribello, G. A.; Banáš, P.; Barducci, A.; Bernetti, M.; Bolhuis, P. G.; Bottaro, S.; Branduardi, D.; et al. Promoting Transparency and Reproducibility in Enhanced Molecular Simulations. *Nat. Methods* **2019**, *16* (8), 670–673.
- (26) Tribello, G. A.; Bonomi, M.; Branduardi, D.; Camilloni, C.; Bussi, G. PLUMED 2: New Feathers for an Old Bird. *Comput. Phys. Commun.* **2014**, *185* (2), 604–613.
- (27) Kärger, J.; Ruthven, D. M.; Theodorou, D. N. *Diffusion in Nanoporous Materials*; Wiley-VCH, 2012.
- (28) Gu, C.; Hosono, N.; Zheng, J.-J.; Sato, Y.; Kusaka, S.; Sakaki, S.; Kitagawa, S. Design and Control of Gas Diffusion Process in a Nanoporous Soft Crystal. *Science* (80-.). **2019**, *363* (6425), 387–391.